Influence of stress, temperature, and strain on calcite twins constrained by deformation experiments

CrossMark

E. Rybacki [a,*], B. Evans [b], C. Janssen [a], R. Wirth [a], G. Dresen [a]

[a] Deutsches GeoforschungsZentrum Potsdam, Potsdam, Germany
[b] Massachusetts Institute of Technology, Cambridge, MA, USA

ARTICLE INFO

ABSTRACT

A series of low-strain triaxial compression and high-strain torsion experiments were performed on marble and limestone samples to examine the influence of stress, temperature, and strain on the evolution of twin density, the percentage of grains with 1, 2, or 3 twin sets, and the twin width—all parameters that have been suggested as either paleopiezometers or paleothermometers. Cylindrical and dog-bone-shaped samples were deformed in the semibrittle regime between 20 °C and 350 °C, under confining pressures of 50–400 MPa, and at strain rates of $\sim 10^{-4}$–10^{-6} s^{-1}. The samples sustained shear stresses, τ, up to ~ 280 MPa, failing when deformed to shear strains $\gamma > 1$. The mean width of calcite twins increased with both temperature and strain, and thus, measurement of twin width provides only a rough estimation of peak temperature, unless additional constraints on deformation are known. In Carrara marble, the twin density, N_L (no of twins/mm), increased as the rock hardened with strain and was approximately related to the peak differential stress, σ (MPa), by the relation $\sigma = (19.5 \pm 9.8)\sqrt{N_L}$. Dislocation tangles occurred along twin boundaries, resulting in a complicated cell structure, which also evolved with stress. As previously established, the square root of dislocation density, observed after quench, also correlated with peak stress. Apparently, both twin density and dislocation cell structure are important state variables for describing the strength of these rocks.

© 2013 Elsevier B.V. All rights reserved.

1. Introduction

Twinning on e-planes $\left\{01\bar{1}8\right\}$ (using the hexagonal structural cell) is common during natural deformation of calcite rocks at temperatures, $T < 300$ °C (Barber and Wenk, 1979). At higher T, twin intensity is reduced, while glide on r-, f-, and c-planes is favored, owing to strong decreases in the critical resolved shear stress (CRSS) for dislocation glide (Barber et al., 2007). Because twins are visually striking and easily measured, they are often used to estimate deformation conditions in rocks containing quartz, calcite, dolomite, or pyroxene (Blenkinsop, 2000; de Bresser and Spiers, 1997; Masuda et al., 2011; Molli et al., 2011; Passchier and Trouw, 1996; Tullis, 1980; Turner, 1953; Wenk et al., 1983, 2006).

Paleopiezometers use twin microstructure to infer either the complete deviatoric stress tensor (Lacombe, 2007; Lacombe and Laurent, 1992; Laurent et al., 1981, 2000), or the magnitude of the difference of the greatest and least principal stresses (Jamison and Spang, 1976; Rowe and Rutter, 1990). The former class uses numerical inversion of twin orientations with constraints from failure or friction criteria, while the latter uses experimentally calibrated relations between twin frequency and stress magnitude. For example, Jamison and Spang (1976) estimate differential stress, σ, by computing the frequency of grains

oriented such that the resolved stress on a given plane exceeds that necessary for twinning, τ_c. That critical value is given by the product of σ and a 'resolved shear stress coefficient', S_1, a function of grain orientation analogous to the Schmid-factor. For randomly oriented grains, Jamison and Spang (1976) calculated the frequency of grains for which $\sigma S_i > \tau_c$ where i indicates 1, 2, or 3 twin sets. In addition to assuming a random orientation distribution, this piezometer treats τ_c as constant and neglects stress inhomogeneities within the solid. In fact, τ_c depends on temperature and strain, ranging from ≈ 15 MPa to less than 5 MPa (de Bresser and Spiers, 1997; Laurent et al., 2000).

Rowe and Rutter (1990) proposed piezometers using three different measures: twin density ($N_L = $ # twins/length), incidence ($I_\tau = $ # twinned grains/# grains total), and volume fraction of twins ($V_\tau = $ volume of twins/total volume). Over the temperature range from 200–800 °C, they found that all three varied directly with stress and were less dependent on temperature, strain, or strain rate; but the latter two also depended on grain size. Their twin density piezometer was

$$\sigma = -52.0 + 171.1 \cdot \log(N_L) \tag{1}$$

where stress was in MPa and twin density in # twins/mm.

All these methods contain assumptions that may limit their applicability (Blenkinsop, 2000; Burkhard, 1993; Ferrill, 1998). Most notably, the approach of Lacombe (2007) and Lacombe and Laurent (1992)

* Corresponding author. Tel.: +49 331 288 1329.
  E-mail address: uddi@gfz-potsdam.de (E. Rybacki).

assumes a constant CRSS for twinning and requires knowledge of rupture and friction laws or of the magnitude of at least one principal stress (e.g., from overburden). Moreover, to get stable results, this piezometer method also rejects incompatible twin sets. Although easier to use, the measures proposed by Jamison and Spang (1976) and Rowe and Rutter (1990) are supposed to be strain-independent, even though calibrations are limited to coaxial mechanical tests done only to low strains <20%. Additionally, most of Rowe and Rutter's experiments were performed in the range 400 °C < T < 800 °C, where deformation mechanisms other than twinning (e.g., dislocation glide) contribute substantial strain. The approaches of Jamison and Spang (1976), Lacombe (2007) and Lacombe and Laurent (1992) assume that τ_c is constant and neglects any dependence on grain-size, temperature, or strain (de Bresser and Spiers, 1997; Laurent et al., 2000). In fact, Ferrill (1998) suggested that stresses inferred for highly strained rocks may be overestimated by a factor of 20.

Twin morphology has also been proposed as a geothermometer for low-grade metamorphic conditions (Burkhard, 1993; Ferrill, 1991; Ferrill et al., 2004). From observations of carbonates deformed along the Swiss Helvetic nappes, Burkhard (1993) proposed a 4-fold classification of twin types to estimate formation temperature. Type I twins are thin (<1 μm), straight, and evolve at T < 170–200 °C; thick (>1–5 μm) type II twins are slightly lensoid, formed at T = 150–300 °C; type III twins are thick, curved, tapered, possibly re-twinned, accompanied by substantial dislocation glide, and occur at T > 200 °C; finally, type IV twins are thick, irregular, accompanied by grain boundary migration, and indicate T > 250 °C (Burkhard, 1993; Ferrill et al., 2004). The classification assumes that twin morphology depends largely on T and only to a minor degree on stress, strain, or strain rate. Hence, twin morphology is often used as a quick and easy geothermometer for the time of deformation (e.g., Janssen et al., 2004).

In the paper, we examined twin production under an extended range of temperatures, stress, and strain by observing the microstructure in carbonate samples from two series of deformation experiments at T < 350 °C to compare the temperatures and stresses in the experiments with those inferred from twin morphology and density, respectively. One set was deformed in coaxial compression to low axial strain, ε < 0.12; the second set was deformed in torsion to shear strains γ of up to 1.8.

2. Experimental and analytical techniques

For most experiments, the starting material was Lorrano Bianco marble from Carrara (Italy), a rock composed of >99% calcite with porosity <0.5%, and a homogeneous microstructure (Coli, 1989). The mean grain size, 220 ± 40 μm, was determined by the line-intercept method, corrected by a factor of 1.5 (Underwood, 1970). Grains have slightly sutured boundaries, but, when viewed in thin section, show little undulose extinction and random crystallographic-preferred orientation verified by electron-backscatter diffraction (EBSD) imaging (L. Morales, pers. communication, 2013). Grains larger than ≈150 μm contain twins >1 μm wide, with a mean twin density of 32 ± 12/mm. Transmission electron microscopy (TEM) shows straight or gently curved dislocations with a density of about 10^{12} m^{-2}. Two additional experiments were done on two other carbonates: fine-grained (7 ± 1 μm) almost untwinned Solnhofen limestone and coarse-grained (720 ± 240 μm) Kunzendorfer marble, which is often twinned in 2 sets with an initial twin density that is about half that of Carrara marble. See Fig. 1 for micrographs of the starting materials.

2.1. Deformation experiments

Using a Paterson deformation apparatus, samples were loaded in triaxial compression resulting in coaxial deformation to low shortening strains, or in confined torsion, resulting in simple shear to large

shear strains (Fig. 2 and Tables 1–2). Details of the apparatus are given by Paterson (1970) and Paterson and Olgaard (2000). For the triaxial compression experiments, we prepared cylindrical samples 20 mm long and 10 mm wide. Samples were jacketed in copper sleeves with wall thickness ≈ 0.3 mm, and deformed without a pore fluid. We performed twelve constant strain rate (velocity) tests to 12% axial strain at confining pressures, P_c = 50–300 MPa, at strain rates, $\dot{\varepsilon}$ = 10^{-4}–10^{-6} s^{-1} and 20 < T < 300 °C (Fig. 3a). Axial force was measured inside the pressure vessel using an internal load cell. Jacket strength was determined by testing non-annealed solid copper samples at similar conditions and subtracted from the measured total force ignoring jacket hardening below about 3% strain. Axial force was converted to true axial stress accounting for sample distortion and assuming constant volume deformation. True (natural) strain and strain rates were determined from axial displacement corrected for system compliance. Error propagation suggests that uncertainties of stress and strain rate are <7% and 3%, respectively. In both the triaxial compression and the torsion tests, temperatures were measured by a thermocouple about 3 mm above the sample and kept constant within ≈2 °C. The temperature gradient along the sample was less than 2–3 °C, confirmed by calibration runs. The precision of the temperature measurements is about 0.5%. One sample was loaded isostatically to P_c = 300 MPa at 200 °C for several hours to examine the effect of heating/cooling and pressurization/depressurization on microstructure.

Torsion tests were performed at P_c = 400 and 370 MPa and T = 50 °C–350 °C (Fig. 3b). Nine samples were deformed at constant twist rate, yielding maximum shear strain rates of 10^{-4} s^{-1} at the periphery of the sample. Two samples were twisted at constant torque, producing a maximum shear stress of about 260 MPa. The applied torque is transmitted from the actuator to the sample only by friction, and, thus, the maximum transferable torque is limited by frictional slippage between the sample and pistons. The yield strength of the samples at low-temperatures is high, so we used cylindrical 'dog-bone'-shaped samples with a reduced diameter in the central part (Fig. 2b). In total, the samples were 30 mm long; the top and bottom sections (s1 and s5) were 15 mm in diameter, and the central section (s3) was 9.2 mm long and either 8 or 10 mm in diameter. Because the total torque applied to a transverse section is constant along the sample axis, and because shear stress increases with an inverse power of diameter, stresses within s3 are much larger than those elsewhere (see Appendix A and Paterson and Olgaard, 2000).

Torque was measured internally by means of an internal load/torque cell, and twist was measured by an external rotary velocity transducer. Samples were jacketed with copper sleeves with wall thicknesses of 0.2–0.4 mm, depending on diameter. The measured twist was corrected for apparatus compliance. Torques were corrected for jacket strength, as determined by calibration tests on low-strength Teflon (polytetrafluorethylene) and Nylon (polyamide) samples, jacketed with copper; by triaxial compression tests on solid copper and using data for the strength of copper (Copper Development Association Inc., Deutsches Kupferinstitut). The calculated strength of copper is between 150 and 80 MPa at T = 50° and 350 °C, respectively, with an uncertainty of 40% that accounts for jacket-hardening persisting at low shear strain (<0.1) and the pre-treatment of Cu-jackets by down-spinning in a lathe at a low rate of feed to ensure that they fit onto dog-bone shaped samples. Due to the relatively low experimental temperatures, jacket strength amounts to about 15% of the measured torque with an uncertainty of about 7%.

To determine the local shear stress, τ, and strain, γ, from measured torque, M, and twist, θ, in torsion tests, we used a simple power law as an approximate description of the mechanical behavior of the rock:

$$\dot{\gamma} = A\sigma^n e^{(-Q)/RT} \qquad (2)$$

where $\dot{\gamma}$ is shear strain rate; n and Q are the stress sensitivity (stress exponent) and temperature sensitivity (activation energy), respectively.
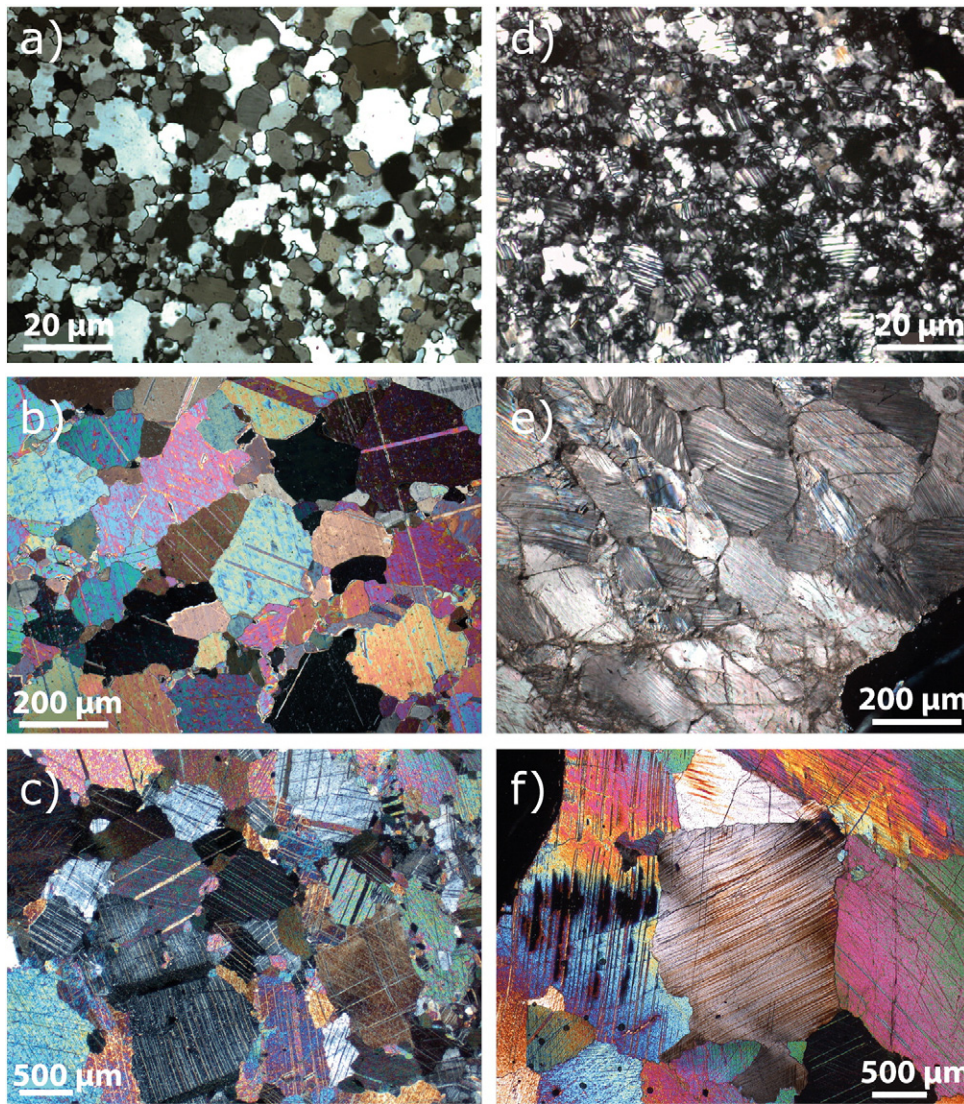
Fig. 1. Optical micrographs of undeformed (left column) and deformed (at $T = 150$ °C, shear strain $\gamma \approx 2$; right column) Solnhofen limestone (a, d), Carrara marble (b, e), and Kunzendorfer marble (c, f). Crossed nicols; note different scales (The interference colors are low order because some thin sections are ultrathin).

R is the molar gas constant, and the pre-exponential factor, A, is a measure of the absolute strain-rate. See the Appendix A for an analysis of stress and strain in samples shaped like a dog-bone.

Departures from steady-state, power-law creep complicate the conversion of torque and twist. During creep deformation of Carrara marble, n and Q are not constant when stress and temperature are varied widely (Renner and Evans, 2002; Rybacki et al., 2003), suggesting that cross-slip (de Bresser, 2002) or glide controlled by lattice resistance (Renner et al., 2002) may be rate-controlling in some conditions. Similarly, at lower T, twinning and microcracking may also lead to mechanical transients (Fredrich and Evans, 1989; Heard, 1960; Rutter, 1972a, b, 1974). The steady-state description is probably least accurate at low temperatures, low pressures, or high strain rates. However, lacking a more detailed mechanical description, we applied Eq. (2) at all conditions. The accuracies of stress and strain measurements during the torsion tests were estimated to be about 9% and 1%, based on sensor precision, uncertainties in the jacket correction and errors in the data conversion.

2.2. Microscopy

We used an optical microscope (Leica DM RX) with an attached high-resolution digital camera (Leica DFC 420) to measure twin density and width in as-received and deformed samples (Figs. 1, 4, and 5). For samples deformed in compression, sections were prepared parallel to the cylinder axis, i.e., parallel to the direction of the maximum compressive stress, σ_1 (Fig. 2a). Stress, strain, and strain rate are nominally constant in this plane. Sections of twisted samples were taken both transverse to the cylinder axis in the section with reduced diameter, and parallel to the long axis near the outer surface of the reduced part. Sections perpendicular to the sample axis and sections parallel to the sample axis are called SR and ST, respectively (Fig. 2b, c). In SR sections, strain and strain-rate increase linearly from the center to the rim, while stress increases non-linearly over the same profile. The distribution of strain and stress within the ST sections depends on the vertical position (see Appendix A and Fig. 4).

Several parameters can be used to characterize twin microstructure, including twin incidence, linear density, width, and twin volume (Rowe and Rutter, 1990). Here, linear twin densities, N_L, were measured on a flat stage by counting the number of twins within individual grains and normalizing by the apparent length perpendicular to the boundary traces. An alternative term for N_L is twin intensity (Ferrill et al., 2004). As shown by Friedman and Heard (1974), twin density estimations using a flat stage match those measured with the universal stage to within 10%. For each axially deformed sample
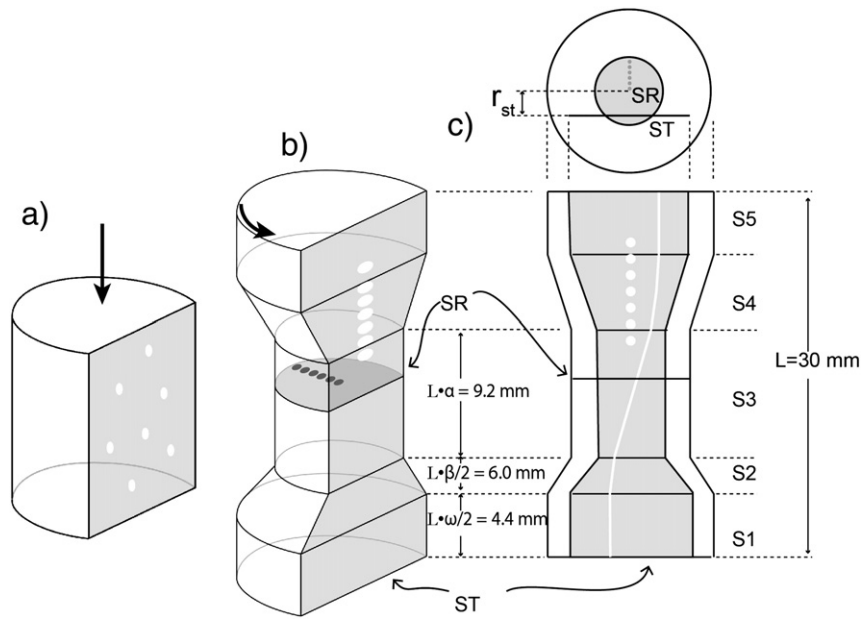
Fig. 2. Sketch of thin section cutting planes for cylindrical (a) and dog bone-shaped samples (b, c). The approximate positions of analysis spots are indicated by white (parallel to sample axis) and dark grey (perpendicular to axis) spots. ST sections are cut parallel to the specimen axis, close to the surface at distance of r_{ST} from the center. SR sections are cut perpendicular to the specimen axis located in the central part, where strain is concentrated (indicated by the white line in c, cf. Fig. A1). The dog-bone-shaped samples of length L and diameter D are reduced in the central part (s3) of fractional length $\alpha \cdot L$ to a fractional diameter of $f \cdot D$. The length fraction of s1 and s5 with diameter D is $\omega/2 \cdot L$ and that of the tapered parts (s2, s4) is $\beta/2 \cdot L$, with $\alpha + \beta + \omega = 1$. For samples with $f \cdot D = 8$ mm, length of s1 = s5 = 4.4 mm, s2 = s4 = 6.0 mm, and s3 = 9.2 mm. For samples with $f \cdot D = 10$ mm, length of s1 = s5 = 3.7 mm, and of s2 = s4 = 6.7 mm. Drawing not to scale.

we calculated the mean twin density at ≥ 10 different positions. For twisted samples, we averaged 4 measurements at each of 9 different positions in ST-sections and each of 6 different positions in SR-sections to account for the spatially varying stress-strain conditions. For ST sections we measured in intervals of 1 mm from the nearly undeformed, top-end

Table 1

Conditions of triaxial compression and torsion experiments on Carrara marble (CM), Kunzendorfer marble (KD), and Solnhofen limestone (SH). 'csr' designates constant strain rate test and 'creep' constant stress test. L is sample length, d is diameter of solid cylinders and of the reduced part s3 for dog-bone shaped samples, respectively, P_c is confining pressure, and T is test temperature. $\sigma_{max}, \varepsilon, \dot{\varepsilon}$, is maximum axial stress, strain and strain rate, $\tau_{max}, \gamma, \dot{\gamma}$ is maximum shear stress, strain and shear strain rate, respectively. Sample CM54 was hot-isostatically annealed without deformation.

Sample	Test	L mm	d mm	P MPa	T °C	Strain rate s⁻¹	Stress MPa	Strain
Triaxial						$\dot{\varepsilon}$	σ_{max}	ε
CM22	csr	20	10	300	20	10^{-4}	446	0.11
CM25	csr	20	10	300	300	10^{-4}	287	0.11
CM34	csr	20	10	300	200	10^{-4}	316	0.11
CM40	csr	20	10	100	200	10^{-4}	278	0.11
CM41	csr	20	10	200	200	10^{-4}	304	0.11
CM46	csr	20	10	300	300	10^{-6}	293	0.11
CMTW03	csr	20	10	100	100	10^{-5}	134	0.0034
CMTW02	csr	20	10	100	100	10^{-5}	187	0.007
CMTW01	csr	20	10	100	100	10^{-5}	236	0.024
CMTW05	csr	20	10	300	100	10^{-5}	243	0.025
CMTW04	csr	20	10	50	100	10^{-5}	229	0.044
CMTW06	csr	20	10	100	200	10^{-5}	237	0.044
CM54	anneal	20	10	300	200	–	–	–
Torsion						$\dot{\gamma}$	τ_{max}	γ
CMDB1	csr	30	10	400	250	10^{-4}	265	1.48
CMDB2	csr	30	10	400	250	10^{-4}	238	0.88
CMDB3	creep	30	10	400	250	$\approx 10^{-3 \cdots -5}$	252	1.16
CMDB4	creep	30	8	400	150	$\approx 10^{-3 \cdots -6}$	266	0.52
CMDB5	csr	30	8	400	150	10^{-4}	284	1.25
CMDB6	csr	30	8	400	50	10^{-4}	262	0.58
CMDB8	csr	30	8	400	350	10^{-4}	208	1.73
KDDB1	csr	30	8	370	150	10^{-4}	210	0.44
SHDB1	csr	30	8	370	150	10^{-4}	264	0.42

to the highly deformed center (Fig. 2). Measurements in the top section were averaged over the first 3–4 intervals. Within zones of highest strain, no measurements were possible owing to extremely fine spacings (apparent linear densities > 500–700 twins/mm). For SR-sections, the measurements started close to the rim and continued in mm intervals towards the opposite side.

In addition, the mean relative frequencies of grains with one, two, or three twin sets were measured to test the piezometer suggested by Jamison and Spang (1976). For triaxially deformed samples, measurements at ≥ 20 positions were averaged. For twisted samples, measurements of ≥ 20 grains at 6 and 9 positions were taken along the transverse and tangential sections, respectively.

If the dip angle of the twin is unknown, the width of an individual twin cannot be measured directly on an ordinary optical microscope with a flat stage. Individual twin widths can be measured using a universal stage to orient the boundaries of each twin perpendicular to the focal plane of the microscope. Thus, we measured twin widths and distances between twins in some samples using universal stage equipment at the Ruhr-University, Bochum (column w in Table 2).

Several other samples were inspected using a flat-stage (column w^* in Table 2). Although individual widths cannot be easily measured on a flat stage, the average width of an ensemble of twins can be determined, provided that measurements include many twins with random dip angles (Underwood, 1970, p. 75). For an ensemble of twins dipping at random angles to the section, the average of the true distances between adjacent boundaries, $w^* = \frac{2}{\pi}\overline{w}_\perp$, where $\overline{w}_\perp$ is the average of the apparent distances measured perpendicular to the traces of the twins in the thin section. More generally, the average distance measured at random angles to the trace of the boundaries on a random thin section, $\overline{w}_r$, is simply $w^*/2$, once again, provided that the boundaries are randomly oriented with respect to the thin section. We categorized between thin (<3 μm) and thick (>3 μm) twins; the exact value to be used is arbitrary, but 3 μm has the virtue of being larger than the resolution limit imposed by optical microscopy and the high birefringence of calcite. For $w^* = 3$ μm $\overline{w}_\perp$ is about 5 μm, an average value that can be easily discriminated using a flat stage at reasonable magnification.

Table 2
Mechanical (strain, equivalent stress) and microstructural (twinning intensity) results. 1 set, 2 sets, and 3 sets designate the percentage of twinned grains exhibiting 1, 2, and 3 twin sets, respectively. N_L is the mean twin (line) density. w and w* are the percentages of twins with width <3 µm estimated from measurements using the universal stage and flat stage, respectively.

Sample	Strain	Equiv. stress MPa	1 set %	2 sets %	3 sets %	N_L mm^{-1}	w < 3 µm %	w* < 3 µm %
CM22	0.11	244	64	36	0	139 ± 58		81
CM25	0.11	166	55	45	0	139 ± 69		31
CM34	0.11	157	65	25	0	139 ± 58		32
CM40	0.11	152	76	14	0	161 ± 65		
CM41	0.11	173	71	29	0	148 ± 113		
CM46	0.11	160	71	24	0	159 ± 65		
CMTW03	0.0034	73	62	38	0	17 ± 10		
CMTW02	0.007	102	80	20	0	24 ± 13		
CMTW01	0.024	129	73	27	0	75 ± 39		
CMTW05	0.025	133	85	15	0	99 ± 43		
CMTW04	0.044	125	86	14	0	116 ± 27		
CMTW06	0.044	130	94	5	0	153 ± 50		
CM54	–	0	29	14	0	18 ± 9		
CMDB1-ST	$5 \cdot 10^{-6}$	81.1	51	31	0	27 ± 20		
	$8 \cdot 10^{-6}$	84.9	24	52	0	21 ± 9	96	
	$4 \cdot 10^{-5}$	99.2	48	48	0	44 ± 23		
	$2 \cdot 10^{-4}$	116.7	75	20	0	62 ± 27		
	$1 \cdot 10^{-3}$	138.4	65	35	0	77 ± 50		
	$9 \cdot 10^{-3}$	165.6	75	25	0	107 ± 46		
	0.19	220.4	65	30	5	750 ± 83		
-SR	1.18	259.2	50	40	10	221 ± 77		22
	0.89	251.8	45	45	10	214 ± 100		
	0.59	241.8	40	50	10	171 ± 68		
	0.30	225.6	46	46	5	63 ± 15		
	~0	~0	50	30	5	103 ± 88		
	0.30	225.6	40	50	0	57 ± 19		
CMDB2-ST	$3 \cdot 10^{-6}$	73.2	41	40	0	30 ± 19		
	$5 \cdot 10^{-6}$	76.6	50	40	0	34 ± 16		
	$2 \cdot 10^{-5}$	89.4	37	56	0	97 ± 23		
	$1 \cdot 10^{-4}$	105.1	46	38	0	216 ± 33		
	$8 \cdot 10^{-4}$	124.6	60	35	0	212 ± 98		
	$5 \cdot 10^{-3}$	148.9	45	55	0	229 ± 65		
	0.11	197.7	30	55	15	761 ± 182		
-SR	0.70	232.5	24	62	14	241 ± 91		
	0.53	226.1	45	50	5	235 ± 82		
	0.35	217.2	46	50	0	193 ± 109		
	0.18	202.6	52	39	0	170 ± 52		
	~0	~0	60	40	0	109 ± 17		
	0.18	202.6	60	35	5	103 ± 52		
CMDB3-ST	$4 \cdot 10^{-6}$	77.2	44	28	0	29 ± 14		
	$6 \cdot 10^{-6}$	80.8	48	48	0	71 ± 41		
	$3 \cdot 10^{-5}$	94.4	65	35	0	72 ± 7		
	$2 \cdot 10^{-4}$	111.0	71	29	0	131 ± 69		
	$1 \cdot 10^{-3}$	131.6	75	25	0	150 ± 56		
	$7 \cdot 10^{-3}$	157.4	62	33	0	288 ± 57		
	0.15	209.3	57	39	4	257 ± 90		
CMDB3-SR	0.93	246.4	50	45	5	187 ± 42		
	0.70	239.5	50	46	4	110 ± 28		
	0.46	229.9	58	25	0	120 ± 39		
	0.23	214.5	67	29	0	134 ± 27		
	~0	~0	48	48	0	83 ± 31		
	0.23	214.5	40	60	0	41 ± 11		
CMDB4-ST	$2 \cdot 10^{-9}$	43.5	45	24	0	23 ± 18		
	$7 \cdot 10^{-9}$	50.3	59	32	0	57 ± 26		
	$1 \cdot 10^{-7}$	65.0	45	50	0	62 ± 23		
	$2 \cdot 10^{-6}$	85.7	75	25	0	101 ± 21		
	$4 \cdot 10^{-5}$	115.7	50	40	10	84 ± 50		
	0.01	190.7	57	33	10	104 ± 27		
-SR	0.39	258.5	45	50	5	201 ± 133		
	0.26	248.2	48	43	0	119 ± 74		
	0.13	231.6	35	61	0	123 ± 49		
	~0	~0	55	45	0	80 ± 45		
	0.13	231.624	35	60	5	133 ± 86		
	0.26	8.2	25	75	0	80 ± 30		
CMDB5-ST	$4 \cdot 10^{-9}$	46.1	45	25	0	15 ± 6		
	$2 \cdot 10^{-8}$	53.3	61	22	0	14 ± 10	98	
	$3 \cdot 10^{-7}$	68.8	40	20	0	23 ± 10		
	$4 \cdot 10^{-6}$	90.8	59	27	0	49 ± 13		
	$1 \cdot 10^{-4}$	122.8	65	26	0	150 ± 57		
	0.03	203.0	64	36	0	333 ± 44		

Table 2 (continued)

Sample	Strain	Equiv. stress MPa	1 set %	2 sets %	3 sets %	N_L mm^{-1}	w < 3 µm %	w* < 3 µm %
-SR	0.94	275.9	25	70	5	394 ± 194		
	0.63	265.0	27	64	9	192 ± 60		
	0.31	247.2	60	30	0	372 ± 82		
	~0	~0	57	43	0	110 ± 67		
	0.31	247.226	45	55	0	185 ± 58		
	0.63	5.0				175 ± 175		
CMDB6-ST	$2 \cdot 10^{-9}$	43.8	53	18	0	15 ± 6		67
	$6 \cdot 10^{-9}$	50.5	50	25	0	57 ± 62	96	
	$1 \cdot 10^{-7}$	65.2	50	25	0	20 ± 5		
	$2 \cdot 10^{-6}$	85.9	63	13	0	34 ± 12		
	$5 \cdot 10^{-5}$	115.7	60	25	0	80 ± 52		
	0.01	189.7				99 ± 43		36
-SR	0.44	254.6	33	57	10	293 ± 139		
	0.29	244.5	70	20	0	142 ± 109		
	0.15	228.1	65	30	0	150 ± 76		
	~0	~0	55	40	0	66 ± 17		
	0.15	228.124	55	35	5	82 ± 51		
	0.29	4.5	48	48	4	82 ± 24		
CMDB8-ST	$6 \cdot 10^{-9}$	32.9	48	43	0	29 ± 7		63
	$3 \cdot 10^{-8}$	38.1	40	45	0	28 ± 8	92	
	$4 \cdot 10^{-7}$	49.3	41	46	0	32 ± 10		
	$6 \cdot 10^{-6}$	65.1	38	52	0	46 ± 21		
	$2 \cdot 10^{-4}$	88.3	45	55	0	103 ± 68		
	0.04	147.1	62	33	0	223 ± 69		19
SR	1.30	202.1	40	50	10	110 ± 43		
	0.87	194.1	48	48	4	124 ± 18		
	0.43	181.1	50	45	5	268 ± 123		
	~0	~0	60	40	0	203 ± 74		
	0.43	181.119	55	35	0	137 ± 24		
	0.87	4.1	24	71	5	84 ± 64		
KDDB1-ST	$7 \cdot 10^{-10}$	33.5	80	20	0	9 ± 3		
	$2 \cdot 10^{-8}$	46.6	67	33	0	12 ± 5		
	$3 \cdot 10^{-7}$	59.6	100	0	0	15 ± 5		
	$2 \cdot 10^{-5}$	90.6	67	33	0	84 ± 7		
	$5 \cdot 10^{-4}$	118.5	75	25	0	67 ± 12		
	0.21	200.5	69	31	0	65 ± 30		
SHDB1-ST	$7 \cdot 10^{-10}$	40.7	0	0	0	0		
	$2 \cdot 10^{-9}$	45.9	0	0	0	0		
	$7 \cdot 10^{-7}$	79.9	0	0	0	0		
	$2 \cdot 10^{-4}$	134.1	0	0	0	0		
	0.14	243.1	<5	0	0	412 ± 148		
	0.20	250.9	<5	0	0	546 ± 320		

For transmission electron microscope (TEM) studies, we cut some sections with a focused ion beam (FIB) microscope (Wirth, 2004, 2009); these were then examined using either an FEI Tecnai™G^2 F20 X-twin TEM or a JEOL 2011 digital microscope.

3. Mechanical behavior

3.1. Triaxial compression experiments

We performed 12 conventional triaxial compression experiments on samples of Carrara marble in the temperature range of 20°–300 °C, confining pressures of 50–300 MPa, and strain rates of 10^{-4} and 10^{-6} s^{-1} (Table 1) (Rybacki and Evans, 1999). All samples hardened up to 11% strain, attaining axial stresses between 130 and 450 MPa (Table 1). To compare mechanical data from torsion experiments to that from conventional triaxial experiments at similar nominal strain rate ($\dot{\varepsilon} = \dot{\gamma}$), we converted the triaxial differential stresses, σ, to equivalent shear stresses using (Paterson and Olgaard, 2000):

$$\tau = \sigma / \left(3^{(1+n)/(2n)}\right) \tag{3}$$

where $n = 10$. This value is likely a lower bound; data from low-temperature axial compression experiments on Carrara marble often give much higher n values. For example, using data from Rutter
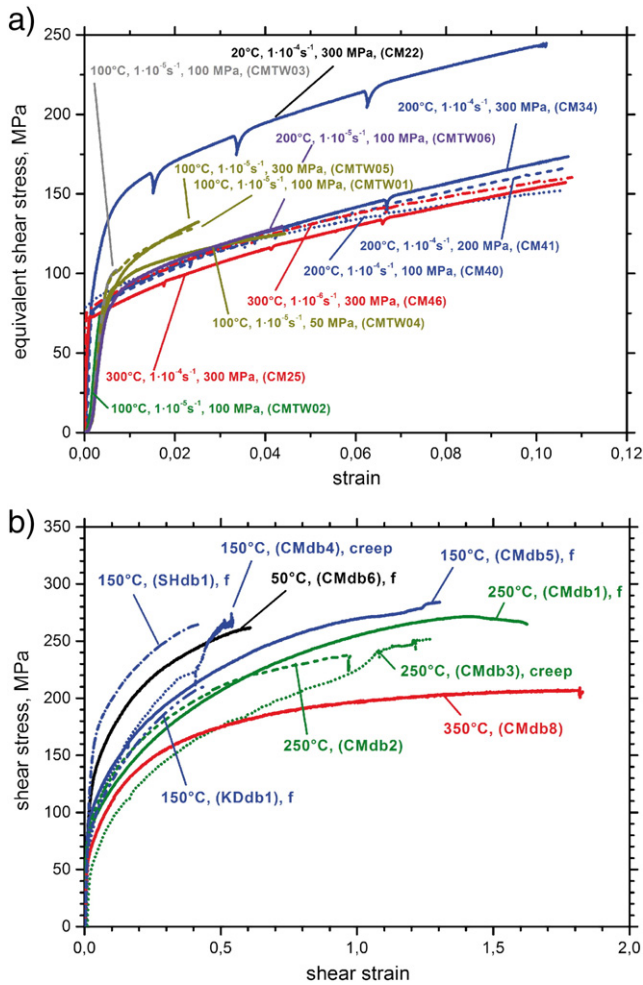
Fig. 3. Equivalent stress-strain curves of deformed carbonate rocks. (a) Triaxial compression tests. Temperature, strain rate, confining pressure, and sample number are labeled for each curve. Small dips in some curves result from partial unloading to determine elastic constants. (b) Torsion tests, performed at 370–400 MPa confining pressure and constant shear strain rates of $1 \cdot 10^{-4} \, s^{-1}$ with the exception of two creep tests as labeled. Temperature and sample number are indicated for each curve; f denotes sample failure.

decelerating to 10^{-5}–$10^{-6} \, s^{-1}$ at the end of testing (Table 1). To calculate equivalent shear stress from measured torque, we also used $n = 10$, producing stresses 1% higher than those obtained using $n = 16$ (cf., Eq. (A1)). The shear stress-strain curves for all torsion tests are shown in Fig. 3b. As in the axial compression tests, equivalent shear stress decreases with increasing temperature. Pronounced strain hardening occurs up to 350 °C. At 150 °C, the strength of the coarse-grained Carrara (CMdb5) and Kunzendorfer marble (KDdb1) samples is similar, but the sample of fine-grained Solnhofen limestone (SHdb1) is distinctly stronger. One sample (CMdB1) showed slight weakening after peak torque at a shear strain of about 1.4.

In five of the torsion experiments, the sample suddenly failed, forming macroscopic fractures oriented at about 45° to the specimen axis and parallel to the direction of maximum compressive stress. The Solnhofen limestone sample displayed multiple cracks inclined by about 45° to the cylinder axis. The mechanical behavior of samples deformed under constant torque is comparable to those deformed at constant twist rate. The slight differences in the torque/twist curves are attributed to the limited response time of the control system and to sample-to-sample variations (Fig. 3b). At a strain of 0.1, equivalent shear stresses obtained in torsion experiments are about 20% lower than those determined from triaxial compression tests. This difference may be related to the underlying assumptions to determine stress from measured torque (see above), or it may result from uncertainties in corrections for jacket strength or machine compliance.

4. Microstructures

Deformed samples show abundant twins, particularly in the coarse-grained marble (Fig. 1e, f). Microfracturing occurs frequently at high strain/stress, particularly at low temperature, but vanishes at 350 °C (Fig. 4). In the fine-grained Solnhofen limestone, twins are not common in grains smaller than about 10 μm (Fig. 1d). The amount of twinning strongly increases with increasing deformation, as illustrated in the central part of ST sections with highly elongated
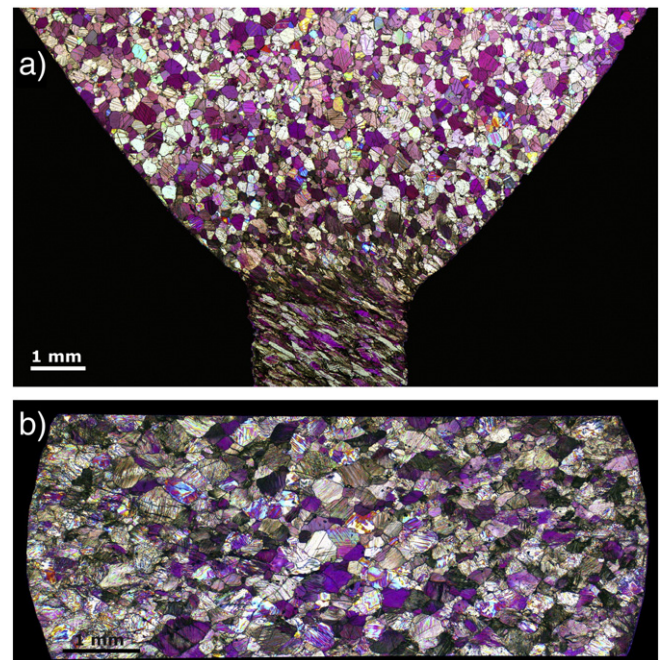
(1974) n is about 16 at $T = 400$–500 °C. Using $n = 10$ results in shear stresses that are 2% smaller than those obtained assuming $n = 16$.

The stress-strain curves for the compression tests (Fig. 3a) show decreasing hardening rates with increasing strain. At a given strain and strain rate, both strength and hardening rates decrease as temperature increases; both increase as confining pressure increases. Such behavior is consistent with semibrittle deformation involving concurrent intracrystalline plasticity and microcracking, as suggested previously (Edmond and Paterson, 1972; Fischer and Paterson, 1989; Fredrich and Evans, 1989; Rutter, 1974). To examine the evolution of the microstructure with strain, we performed several tests at almost the same stress to different total strains (samples CMTW01, CMTW05–06). In addition, two samples were loaded to just below and above the aggregate yield point (samples CMTW03 and CMTW02).

3.2. Torsion experiments

Five Carrara marble samples, one Solnhofen limestone sample, and one Kunzendorfer marble sample were deformed at constant twist rate and temperatures of 50–350 °C under confined torsion. The nominal strain rate at the outer surface of the reduced section of the dog-bone samples was similar to that in the axial compression tests. Two additional tests on Carrara marble samples were performed at constant torque, resulting in maximum shear strain rates $\approx 10^{-3} \, s^{-1}$,

Fig. 4. Photomicrographs of twisted sample CMDB5, deformed at $T = 150$ °C to $\gamma = 1.25$, showing an increase of twinning intensity with increasing deformation, i.e. from top (s1) to bottom (s3) in the ST-section (a) and from the center to the rim in the SR-section (b). Crossed nicols.
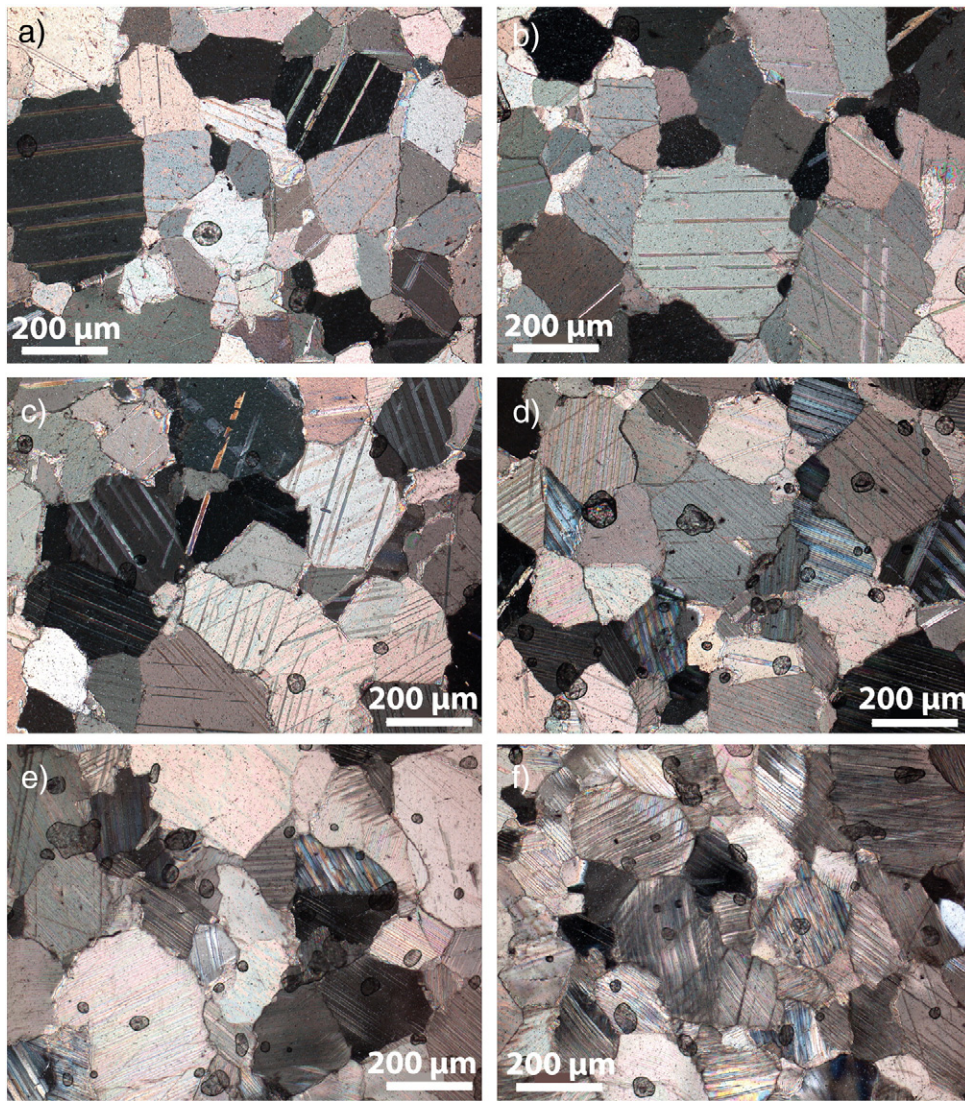
Fig. 5. Thin section micrographs of deformed sample CMDB5, revealing increasing twinning intensity and occurrence of multiple twin sets with increasing stress and strain, respectively. From (a) to (f) shear strain and stress increases from 0 to 0.03 and from 46 MPa to 203 MPa, respectively (cf., Table 2). The locations of each micrograph are shown approximately (from top to bottom) by the white spots indicated in Fig. 2. Crossed nicols. Note bending of twin-planes at high stress/strain.

grains (Fig. 4a; Fig. A1), and across SR sections, where stress and strain increase from the center towards the outer rim (Fig. 4b; Fig. A2). Also, with increasing deformation, the number of grains with multiple twin-sets increases and bending accommodates strain at the more strongly twisted portions (Fig. 5). Here, twin densities are very high and difficult to count using optical microscopy.

4.1. Twin densities and percentage of twinned grains

Linear twin densities, relative frequencies of grains with 1, 2, or 3 twin sets, and frequencies of thin and thick twins, along with the experimental conditions are given in Table 2. To compare the two types of mechanical tests, the differential stress measured during axial compression is converted to equivalent shear stress (Eq. (2)). For the dog-bone torsion samples, we calculate the local equivalent shear strains and stresses, as outlined in the Appendix A, assuming $n = 10$.

Grains from torsion tests on Carrara marble often exhibit one (24–71%) or two (13–71%) twin sets; grains with three sets are much scarcer (0–15%). All grains of the deformed Kunzendorfer marble are twinned in 1 or 2 sets. In the strongly deformed sections of the

Solnhofen limestone sample, a few of the larger grains are twinned in one set (Table 2). No grains in the axially deformed samples have three sets. The relative frequency of grains with thin twins is between 19 and 98%, depending on stress and strain conditions.

Linear twin densities vary from 15/mm to 760/mm, with scatter sometimes exceeding 50%. The twin density of sample CM54, which was annealed under isostatic pressure, is about 30% less than in the starting material, but still comparable within error. Thus, it is unlikely that depressurization or cooling after deformation modifies twin density by a large amount. A linear regression of log (N_L) versus log (equivalent stress) yields

$$\log(\tau) = 1.17 \pm 0.08 + (0.49 \pm 0.04) \cdot \log(N_L) \qquad (4)$$

where τ is in MPa, and N_L is the # of twins/mm (dotted-dashed line in Fig. 6). The slope of the fit is mainly determined by the twin-density distribution in the tangential (ST) sections (open symbols) where the strain is low. In fact, the stress in some of these areas may have been below the macroscopic yield point of the aggregate ~75 MPa (Fig. 3). Assuming that the local stress in these areas can be calculated from the elastic moduli ignoring grain-scale stress perturbations, then

the slope of the fitted line is increased by $\approx 18\%$ and the intercept is decreased by about the same amount, but both changes are below statistical significance.

When twin density is larger than 200 twins/mm (or 1 twin/5 µm), measurements using optical microscopes are quite difficult because of limitations in resolution and the presence of interference fringes (Groshong, 1972). In addition, at high stress and twin density, boundaries are often bent or slightly sutured. If the analysis is limited to data where $\tau < 140$ MPa (dotted line in Fig. 6), or, equivalently, $\sigma < 250$ MPa, which maybe a reasonable limit for geological conditions at the investigated temperature range, then the corresponding regression with the slope fixed at 0.5, yields

$$\log(\tau) = 1.03 \pm 0.02 + (0.50 \pm 0.05) \cdot \log(N_L) \qquad (5)$$

(solid line in Fig. 6), where the error in slope is adopted from Eq. (4). The corresponding piezometer in terms of differential stress is

$$\log(\sigma) = 1.29 \pm 0.02 + (0.50 \pm 0.05) \cdot \log(N_L). \qquad (6)$$

Notice that twin densities for the fine-grained Solnhofen limestone fit the regression line, if extrapolated to lower stresses. Also, the coarse-grained Kunzendorfer marble appears to follow a similar stress–twin density relationship within errors, probably with a slightly different offset. It may be that the piezometer is independent of grain size, but that a threshold stress is necessary to activate twinning in the fine-grained limestone, which didn't show twins at low stresses (Table 2). The formal statistical errors of the regression in Eq. (5) are ± 0.02 and 0.05 for the offset and slope, respectively, but actual local measurements of microstructure vary more substantially than that. In addition to errors in measurement of microstructure, additional uncertainty is added by the inaccuracies in the location of the measurements, in the jacket strength correction, and in the choice of n. Reduction in measurement error can be achieved by making multiple twin density measurements to minimize the influence of the dipping angle for arbitrary oriented twins on the density estimation, and this redundancy is certainly recommended. Based on the scatter of the data, a more conservative and realistic estimate of uncertainty is $\Delta\log(\tau_0) = \pm 0.2$. Thus, the real accuracy of stress estimates from twin density is probably $\pm 50\%$, or

$$\sigma = (19.5 \pm 9.8)/\sqrt{N_L}. \qquad (7)$$

The twin density also appears to depend on strain that may additionally account for the large data scatter. This relationship is apparent if the data are separated into groups characterized by temperature and loading condition, i.e., triaxial or torsion, constant torque or twist-rate (Fig. 7). At temperatures below 350 °C, N_L increases with strain, in particular at low T and low shear strain 0.5 (Fig. 7a–c). At the highest temperature (350 °C), twin density in the high-strain radial sections is either constant or negatively correlated with strain (Fig. 7d). In triaxial deformation, density does not change abruptly just above the yield point, but steadily increases up to 5% strain, even when stresses are similar (Fig. 7e, Table 2). In all these examples, the scatter in the data is large and more refined observations are necessary to clarify this point.

4.2. Twin thickness and morphology

We also measured the frequency of apparently thin ($w^{(*)} < 3$ µm) and thick ($w^{(*)} > 3$ µm) twins in selected Carrara marble samples, covering a range of stress and strain conditions (Table 2). Thick twins include those with curved or sutured boundaries. The apparent widths were collected into only two bins because actual twin thicknesses were not measured. The torsion data are separated into sets from nearly undeformed sections (strains $< 10^{-5}$, Fig. 8a) and sections strained up to $\gamma = 1.2$ (Fig. 8b). The frequency of thick twins in more deformed samples is

about 40% higher than in those that are nearly undeformed. Thus, notwithstanding the uncertainty in twin width, the frequency of thick twins seems to be a function of both temperature and strain. Generally, thick twins become more abundant with increasing stress up to about 150 MPa, independent of temperature, excepting the 20 °C-sample.

4.3. Dislocation activity

Because twinning is accompanied by dislocation generation and motion, even at relatively low temperatures, it is important to observe changes in dislocation microstructure as the carbonates are deformed. Thus, we prepared 4 FIB-sections from sample CMDB5, deformed at 150 °C. The foils were taken at 3 different positions along the tangential section and at 1 position near the rim of the radial section, reflecting different stress/strain conditions. In a slightly deformed tangential section where $\tau = 46$ MPa, dislocation density (line length/volume) is $2.2 \cdot 10^{12}$ m^{-2}, similar to that of the undeformed marble (Fig. 9a). At a slightly higher stress of 69 MPa (just below the macroscopic yield stress of ~75 MPa), dislocation density is unchanged within errors (~$1.4 \cdot 10^{12}$ m^{-2}). At 131 MPa, the dislocation density was high enough, $8 \cdot 10^{13}$ m^{-2}, that it was difficult to count the free dislocations (Fig. 9b). At the highest stress, 281 MPa, the dislocation density was more than $1.6 \cdot 10^{14}$ m^{-2} (Fig. 9c).

Dislocations are present within the twin volume, but they also accumulated at the twin boundaries, forming tangled structures of higher density. The high-density tangles sometimes show ladder-like patterns, as, for example, in sample CM22, deformed at room temperature to an equivalent stress of 258 MPa (Fig. 9d). These cell structures are reminiscent of the microstructures in cold-worked, strain-hardened metals that are often associated with the development of persistent slip bands and twinning (Marinelli et al., 2006). As might be expected, increasing stress decreased the size of the cells. In one case, the interaction between the partial twin boundaries and several pores resulted in an echelon configuration (Fig. 9c).
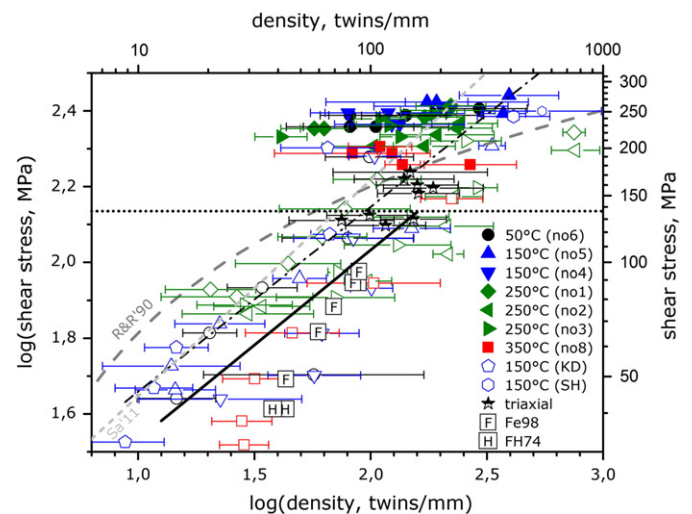

Fig. 6. Twin density versus applied shear stress in double-logarithmic scale. Closed and open symbols denote results from SR- and ST-sections of twisted Carrara marble, Kunzendorfer marble (KD) and Solnhofen limestone (SH) samples, respectively, and half-filled stars show data from triaxial compression tests. Dotted-dashed line shows regression fit of all data (Eq. (4)) and solid line shows fit (Eq. (5)) of data below about 140 MPa shear stress (dotted horizontal line). Lines labeled R&R'90 and Sa'11 show twin density-based piezometers suggested by Rowe and Rutter (1990) and Sakaguchi et al. (2011), respectively. F-symbols show data collected by Ferrill (1998) on Indiana limestone at $T = 20$ °C, $P_c = 100$ MPa, and H-symbols represent compression data on Gulf coast limestone measured at $T = 150$ °C, $P_c = 100$ MPa, and $\sigma = 75$ MPa (Friedman and Heard, 1974).

5. Discussion

Twinning is an important strain mechanism active in carbonate rocks at low temperatures (Groshong, 1972, 1988), playing a role similar to dislocation glide (Astafurova and Chumlyakov, 2009; Barnett, 2007; Beyerlein and Tomé, 2008; Burkhard, 1993; Turner et al., 1954) by providing strain elements necessary to satisfy the von Mises condition. Twinning is particularly important during high-pressure deformation of low symmetry crystals. For a comprehensive general review, see Christian and Mahajan (1995); for reviews of twinning in calcite, see Burkhard (1993); Ferrill et al. (2004); and Turner (1964).

5.1. Inter-relationship of strength and twinning in calcite at low temperatures

Twin nucleation begins early in the loading cycle (Garber, 1947; Klassen-Neklyudova, 1964), most likely at stress concentrations on crystal surfaces, on grain boundaries, or near other defects. Once nucleated, twins grow rapidly as twin dislocations glide along planes parallel to the twin boundary (Burkhard, 1993; Christian and Mahajan, 1995; Nicolas and Poirier, 1976). Optical observations and the presence of intermittent load drops during deformation of single crystals at elevated temperature (de Bresser and Spiers, 1993; Garber, 1947) suggest that the stress to cause glide of twin dislocations in calcite is small compared with that necessary to nucleate them, at least when back stresses from other defects are small. Optical observations in calcite single crystals (Reusch, 1867; Williams and Cahn, 1964) and neutron diffraction experiments in polycrystalline limestone (Covey-Crump and Schofield, 2009) show that twins may nucleate and grow even when the applied stress is below the aggregate yield point. In these cases, when the load is removed, strain vanishes, and, thus, deformation is reversible.

At loads greater than the aggregate yield point, twin strain is inelastic, owing to repulsive interactions between twin dislocations and matrix defects, e.g., cracks, dislocations, and other twins, all of which may hinder reverse motion of twin boundaries (Klassen-Neklyudova, 1964). Conversely, twin boundaries are obstacles for dislocation slip (cf. Christian and Mahajan, 1995). As an example, our TEM observations show increased dislocation density near the twin boundaries. Often the matrix dislocations are arranged in cell-like networks suggesting repulsive interactions between twins and the dislocation structure (Fig. 9). Such negative interactions result in strain hardening, during which both dislocation slip and twin growth are made more difficult, and, indeed, some previous workers have suggested that the stress necessary for twin production in calcite depends on strain (e.g., de Bresser and Spiers, 1997; Laurent et al., 2000).

Analysis of strain hardening during mechanical tests can be used to gauge the interactions between the mechanisms of inelastic deformation (Beyerlein and Tomé, 2008; Gil Sevillano and de las Cuevas, 2012). When calcite is deformed at low T in the laboratory, hardening rates increase with either increasing confining pressure or decreasing temperature (Fischer and Paterson, 1989; Fredrich and Evans, 1989; Heard, 1960; Rutter, 1972a, 1974; Rybacki and Evans, 1999) and change with strain at fixed $\dot{\varepsilon}$, T, and P_c. The average hardening rate over the initial 10% strain interval in our conventional triaxial deformation tests was about 0.8–0.9 GPa/strain at room temperature, decreasing to about 0.5 GPa/strain over the same strain interval and confining pressure at 300 °C. These hardening rates are about 2% of the shear modulus of calcite, a ratio similar to that was found during twinning-induced plasticity in Fe–Mn alloys (Gutierrez-Urrutia and Raabe, 2011). The mechanical curves for torsion suggest that hardening rates decrease at larger strains. Using Eq. (7), hardening rates (cf. Fig. 3) can be compared to the rate of increase in N_L observed in the same experiments (Fig. 7). At temperatures up to 150 °C, the average aggregate hardening rates overestimated the observed increase in N_L, but became nearly equal to the observed changes at 250 °C, which is improved when taking into account the non-linear decrease of hardening rates with strain. However, at 350 °C, the twin density appeared to

decrease with strain (Fig. 7d) although strain hardening still persisted. The uncertainties in the measurements are quite large, but if these observations are confirmed by more detailed measurements, then they may suggest that as T increases, the hardening owing to twin production is decreasing at a rate faster than the hardening resulting from interactions among the matrix dislocations. However, it is important to remember that microfracturing may also often occur concurrently with creep deformation in carbonate rocks, particularly when the differential stress is nearly as large as the effective confining pressure (Heard, 1960). Both strength and hardening are affected by strain partitioning among cataclasis, creep, and twinning, and, here, the influence of cataclasis has been ignored.

5.2. Twin widths, strain, and geothermometers

The strain in a rock that can be associated with twinning is determined by several factors, the most important being the total fractional twin volume produced during deformation, V_V (Ferrill et al., 2004; Groshong, 1972; Chapter 8 in Kocks et al., 1998); other factors include the shear strain produced by each twinning event, the distribution of grain orientations, and the loading geometry. V_V is equal to the product of the number of twins per unit volume of rock, N_V, and the average volume of all the twins, $\overline{V_{twin}}$ (Ferrill et al., 2004; Groshong et al., 1984). For example, for a randomly oriented assemblage of oblate spheroids with average length, l, thickness, t, and aspect ratio, $q = t/l$, is

$$V_V = \frac{\pi}{6} N_V q l^3.$$

When q is less than 0.4, V_V is approximately

$$V_V \approx \frac{t \cdot N_L}{(0.54q + 0.72)}. \tag{8}$$

(Barnett et al., 2012; Dehoff and Rhines, 1961; Underwood, 1970). Using the correlation between the product of twin density and twin volume, Groshong (1972, 1974) and Groshong et al. (1984) developed a technique to measure twin strain in naturally deformed rocks.

Earlier triaxial deformation tests done at room temperature on samples of Indiana limestone (Ferrill, 1998; Groshong, 1974; Jamison and Spang, 1976) indicate that twin density increases with strain, but that twin widths increase only very slowly (or not at all) with strain at low T. In our experiments, strain apparently correlated with both the number of twins and their average widths at all temperatures (Figs. 7–8). The relation between width and total strain, however, is not well-constrained from these experiments, because the width data are approximate, and the production of thick twins is inferred from a simple comparison between nearly unstrained rocks and those subjected to strains of ≥0.01 (Fig. 8). For example, we cannot distinguish between widening of thin twins during deformation or the nucleation and growth of wide twins in a single burst. Clearly, more detailed data are needed.

Observations of microstructures in naturally strained carbonates suggest that twin morphology can be used to constrain the temperature of deformation (Burkhard, 1993; Ferrill et al., 2004; Groshong et al., 1984). Thick twins predominate above about 200 °C, while twins formed below that temperature tend to be thinner. It should be noted that the twin-morphology geothermometer limits the occurrence of thick irregular twins with sutured boundaries (type IV) to temperatures >250°, but some field observations suggest that the onset of recrystallization of calcite with mobile twin boundaries may occur at temperatures as low as 150–250 °C (Kennedy and White, 2001).

The tendency to develop thicker twins at higher T can be rationalized by considering the physical mechanisms of inelastic deformation. Twin broadening should be aided by dislocation recovery, which would reduce
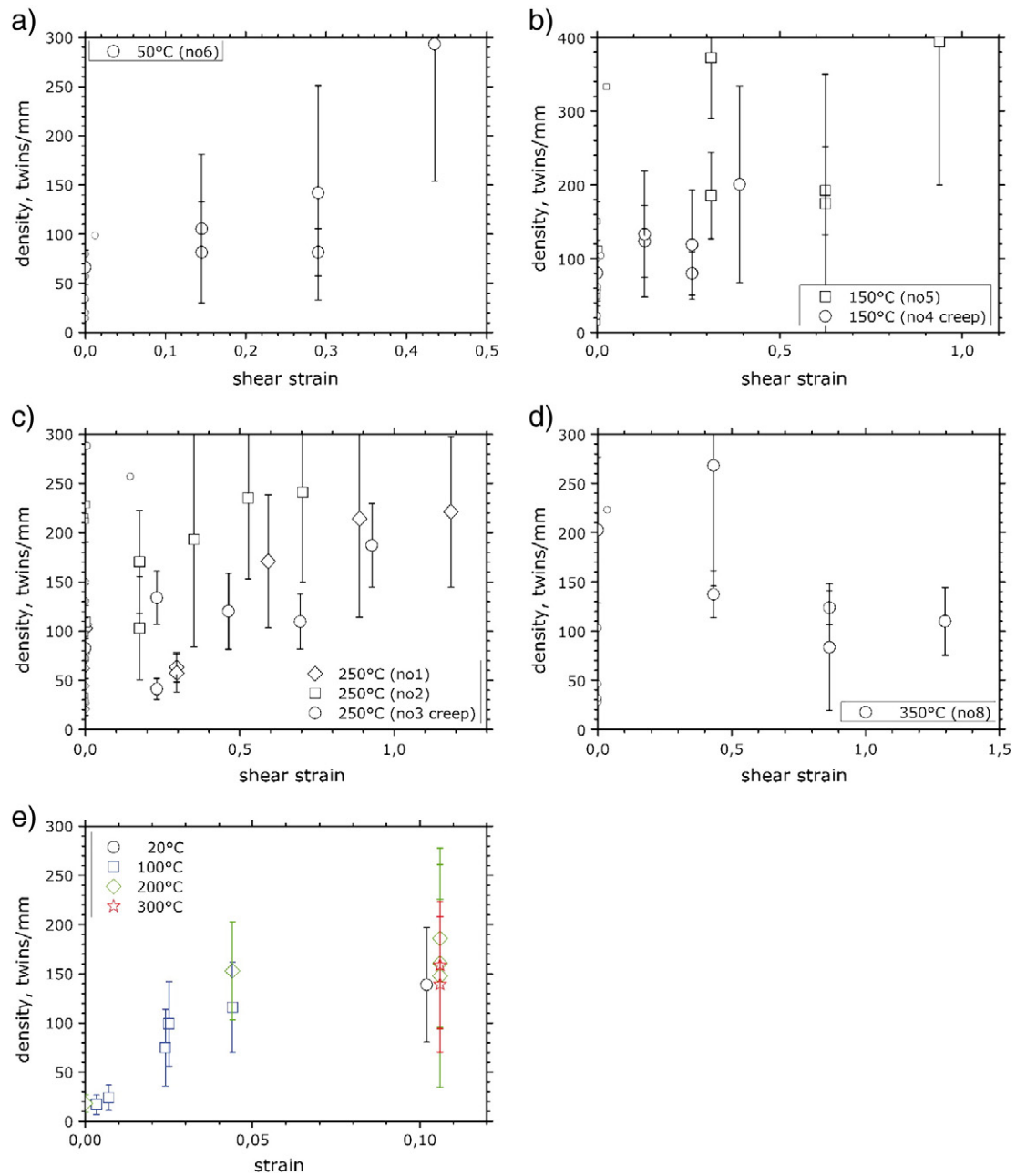
Fig. 7. Twin density versus strain for samples twisted at (a) 50 °C, (b) 150 °C, (c) 250 °C, (d) 350 °C, and for triaxially deformed samples (e). Note that for twisted samples increasing strain is associated with increasing stress, owing to strain hardening.

repulsive interactions between twin dislocations and the matrix dislocations. Dislocation recovery mechanisms, grain boundary migration, or boundary sliding are other processes that might relieve strain incompatibilities when twins ending in one grain impinge on neighboring grains. All these processes are favored by higher temperature and lower strain rates. The processes of twin nucleation and broadening likely have different kinetic laws, and, thus, the relative rates of the two may change with deformation conditions or from one material to another. For example, in Cu–Zn alloys deformed at low T, the twin thickness decreases slightly with increasing strain and with a decreasing Zener–Hollomon parameter, Z, where $\ln(Z) = \ln(\dot{\varepsilon}) + \frac{Q}{RT}$ (Xiao et al., 2008). In pure nano-twinned copper, twin width is independent of Z, but N_L increases with higher Z (Li et al., 2009). Finally, Rowe and Rutter (1990) suggested that the average twin width increased linearly with grain size, d. Thus, although temperature might be the major influence determining twin

width, average widths might be also influenced by changes in strain, strain rate, or grain size.

5.3. Twin density and paleo-piezometers

In the range $\tau < 140$ MPa, the twin density piezometer given by Rowe and Rutter (1990) is an upper bound of our measurements (Fig. 6), but data from our triaxial compression tests done at higher stresses and lower strains (stars in Fig. 6) plot close to Rowe and Rutter's piezometer and our low stress regression line. Twin densities collected by Ferrill (1998), using data measured by Groshong (1974) and Jamison and Spang (1976), lie below Eq. (7) at low stresses, but all three curves are still within the large experimental error (Fig. 6). It is important to note the differences in experimental techniques. Our data came from tests at $23 < T < 350$ °C, in both conventional
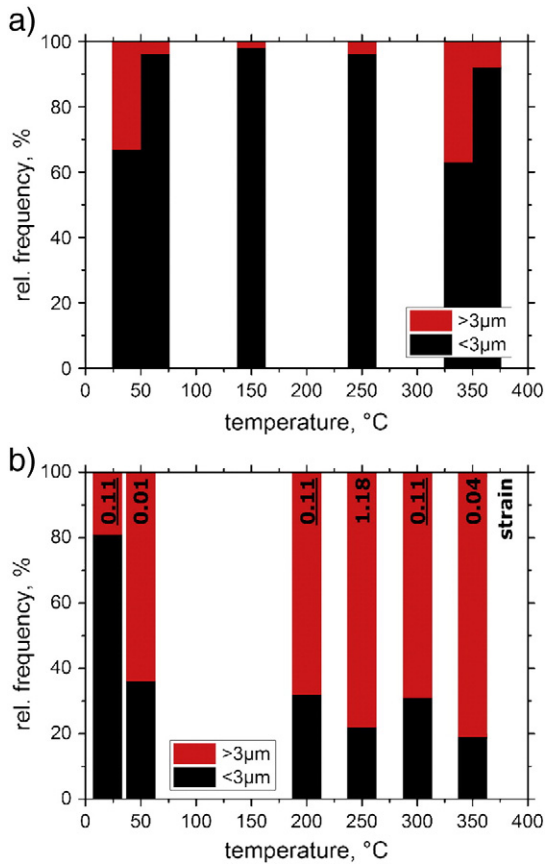
Fig. 8. Relative frequency of thin (<3 μm) and thick (>3 μm) twins in deformed Carrara marble versus temperature at negligible strain (<10⁻⁵) (a) and high strain (b).

triaxial and torsion (simple shear) loading up to high strain, with confining pressures (P_c) up to 400 MPa. Rowe and Rutter (1990) performed low-strain, axial-compression experiments on dense samples of Carrara and Taiwan marble at 400° < T < 800 °C and P_c = 100 MPa. Ferrill (1998) used porous Indiana limestone deformed to strains of 6% at room temperature and confining pressure of 100 MPa, which can be approximated by a stress–twin density relation of $\sigma = 3.52 \cdot N_L^{0.86}$, giving in log–log scale a lower offset and higher slope compared to our results. Friedman and Heard (1974) performed low stress/low strain (<0.02%) creep tests on a relatively dense Gulf coast limestone in confined extension and compression at temperatures and pressures of 24 °C and 0.1 MPa; 75 °C and 50 MPa; and 150 °C and 100 MPa. Their data plot also below Eq. (7), fitting approximately to those of Ferrill (1998) at 150 °C and an applied σ of 75 MPa, i.e. close to the yield stress (Fig. 6). Interestingly, no significant difference was found in twin density development between compression and extension tests, but at very low differential stress (≤40 MPa) twin density increased from twice that of the starting material after 10 min at constant load up to 7 times after 4000 min duration, even though no permanent strain was measured. This result is in contrast to our observation that the twin density is hardly changed below the yield stress in coarse-grained Carrara marble (cf. samples CMTW02, CMTW03). Taking these observations together suggest that for fine-grained limestones the twin-density is less affected by the magnitude of peak differential stress, which is probably associated with additional deformation mechanisms like grain boundary sliding acting in fine-grained limestone.

Recently, Sakaguchi et al. (2011) performed triaxial compression tests on sandstone containing 0.5 vol.% calcite grains with an average grain size of 130 μm. Samples were loaded to differential stresses of 0, 209, 400, 542, and 685 MPa under P_c = 115 MPa at 200 °C. Subsequent measurement of twin lamellae (mostly less than 1 μm thick) in the calcite grains was used to fit a stress–twin density relation of the form $\sigma = 21.86 \cdot \rho^{0.57}$. Below 250 MPa, this relation yields stresses about 50% higher than Eq. (7) (Fig. 6). There are several factors with unknown effects on the twin density/stress relation. These include the influence of non-coaxial strain, of compaction and dilation (and, hence, pressure), and of local stress perturbations near a stiffer phase or near a large pore. In tests with relatively low confining pressure (relative to axial load), twin density appears to be larger at a given stress, but, once again, the large scatter in data prevents definite conclusions.

In the dense carbonate rocks tested here, flow stress was roughly proportional to the square root of twin density (Eq. (7); Fig. 6). Such behavior would be consistent with models where twin boundaries are regarded as barriers for dislocation slip (Beyerlein and Tomé, 2008; Capolungo et al., 2009; Gutierrez-Urrutia and Raabe, 2011,
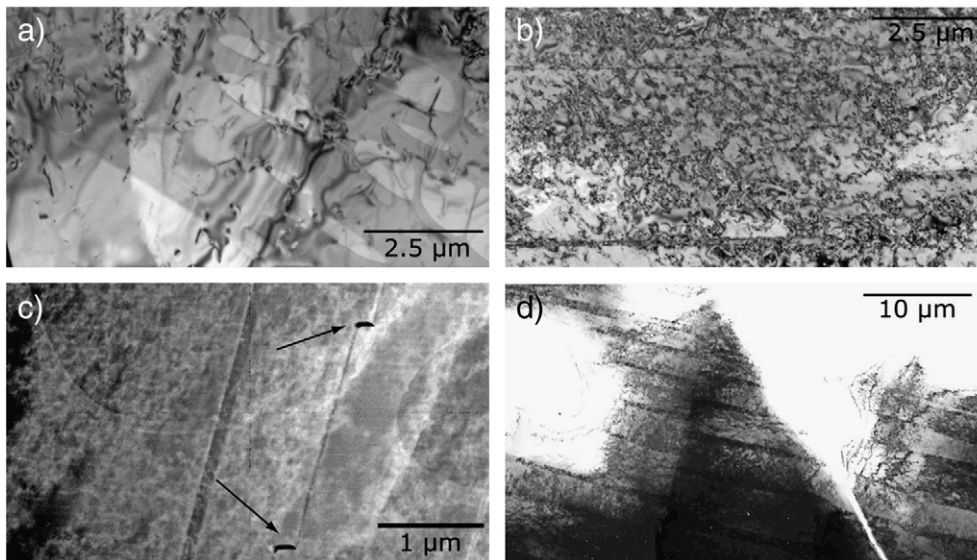

Fig. 9. TEM micrographs of twisted sample CMdb5 showing increasing dislocation densities with increasing stress from 46 MPa (a), to 131 MPa (b) to 281 MPa (c). (d) shows dislocation networks in sample CM22, axially deformed at an equivalent stress of 258 MPa. Note formation of dislocation cells at high stress and interaction of twins (arrows in c). (a), (b), and (d) are bright field images, (c) is a high angle annular dark field image.

2012). Then, decreases in twin plane spacing would decrease the mean free path for slip of matrix dislocations and harden the material. And, thus the stress necessary for matrix slip would increase with $\sqrt{N_L}$. Such a relation has been suggested for hardening in TWIP steel alloys (Gutierrez-Urrutia and Raabe, 2011). But, notice that the mean free spacing between twin planes will also be affected by the twin width. Thus, a simple relation between applied stress and N_L would be complicated by large variations in t.

The relationship between twin density and stress is also formally similar to the Taylor relation between stress and dislocation density, ρ_d,

$$\tau = \alpha \mu b \rho_d^{0.5} \qquad (9)$$

with μ = shear modulus, b = length of the Burgers vector and α is a constant close to 1 (Karato, 2008; Kohlstedt and Weathers, 1980; Poirier, 1985). Based on uniaxial compression tests on calcite single crystals at 550°–800 °C, where slip occurs largely on r- and f-glide systems, de Bresser (1996) obtained a slightly different piezometer:

$$\sigma[MPa] = 10^{-6.21} \rho_d^{0.62} \left[m^{-2} \right] \qquad (10)$$

or, when converted to equivalent stress

$$\log(\tau[MPa]) = 0.97 + 0.62 \cdot \log \left(\rho_d \left[\mu m^{-2} \right] \right). \qquad (11)$$

These empirical relations also hold for polycrystalline calcite at stresses >40 MPa and ε > 2%.

Using Eq. (11), we compare stresses estimated from free dislocation density in sample CMDB5 with those calculated from the applied torque. When the applied stress is larger than the CRSS for r- and f-glides at 150 °C (60 and 100 MPa, respectively de Bresser and Spiers, 1997), the dislocation data are consistent with de Bresser's (1996) piezometer (Fig. 10).

A second microstructural parameter, dislocation cell size, d_c, is expected to be inversely proportional to shear stress,

$$d_c = \frac{K\mu b}{\tau - \tau_o} \approx \frac{K\mu b}{\tau} \qquad (12)$$

where K is a constant (of about 3–4 for slip bands) and τ_o is the lattice friction stress (Ananthakrishna, 2007). Applying this relation to cell sizes in Fig. 9 gives the relationship

$$\tau[MPa] = \frac{47.9}{d_c[\mu m]} \qquad (13)$$

which, however, is based on only 4 data points (Fig. 10). Using μ = 39.2 GPa and $b = 6.4 \cdot 10^{-10}$ m for calcite (de Bresser, 1996) yields a constant, K, of about 2. Formal comparison of these relationships (twin density, dislocation density, and dislocation cell size) suggests that the three microstructural variables should scale as $N_L \sim \rho_d{}^n \sim d_c^{-2}$, where n is 1–1.2.

5.4. Twin frequency and paleo-piezometry

In Fig. 11, we compare equivalent shear stresses present during compression and torsion to those estimated from the twin-frequency piezometer (Jamison and Spang, 1976) assuming τ_c = 10 MPa. Equivalent stresses in the torsion experiments were calculated using Eq. (3) and n = 10. A few data points yielded stress values > 300 MPa, but these are not shown. In both the axial compression and torsion experiments on Carrara marble, more than 90% of grains contain at least one twin set, and thus, stress can be estimated only from the 2- and 3-twin frequencies. For samples deformed in triaxial compression (Fig. 11a), stresses estimated from the 2-twin set frequency are
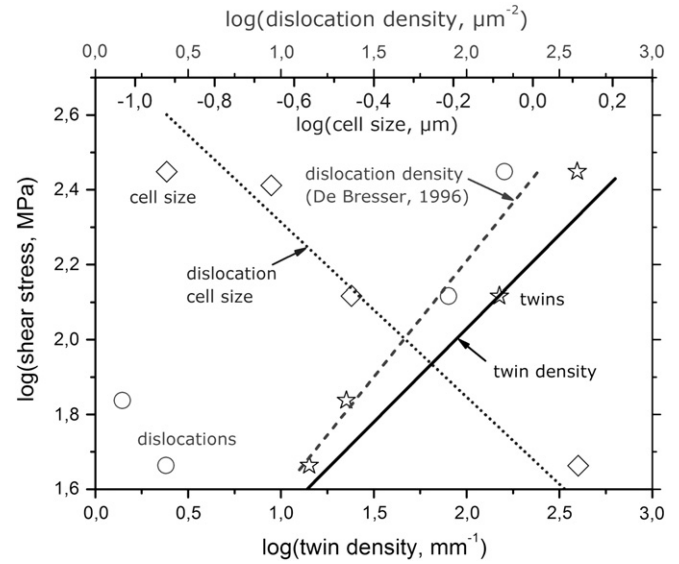

Fig. 10. Comparison of twin density (stars) and dislocation density (circles) of sample CMDB5. Solid and broken lines show the twin density (Eq. (5)) and dislocation density (Eq. (11)), de Bresser, 1996) piezometers, respectively. Diamonds and dotted line (Eq. (13)) represent the approximate dislocation cell size of samples shown in Fig. 9.

significantly underestimated (typically by about 100 MPa) with no systematic correlation to temperature, pressure, or strain rate. Similarly, in the torsion experiments, the local equivalent stress estimated from microstructure is usually lower than that calculated from applied torque, independent of changes in temperature (Fig. 11b). Estimates based on 3-twin sets predict stresses even lower than those shown. Thus, the twin-frequency piezometer is, at best, a lower bound for our data.

In contrast, for fine-grained limestone samples shortened by 4–5% in axial compression, the predicted stresses (Ferrill, 1998; Jamison and Spang, 1976), using the 1- and 2-set frequencies, were higher than that applied, i.e., frequencies were greater than expected. This result is contrary to the common expectation that rocks with smaller grains will tend to have fewer twins at the same macroscopic applied stress (Passchier and Trouw, 1996). Also, notice that the results for the Kunzendorfer marble loaded in torsion are similar to those for Carrara marble (Fig. 11b). Thus, the effect of grain size on the frequency piezometer is quite uncertain.

The twin-frequency piezometer is very sensitive to the choice of the CRSS for twining, τ_c. For example, if τ_c = 30–40 MPa is used (Laurent et al., 1981) instead of 10 MPa (Ferrill, 1998; Jamison and Spang, 1976), applied stresses are overestimated for Carrara marble.

The CRSS for twinning in single crystals depends weakly on temperature, and these results and earlier studies suggest that the stress necessary for twin production in polycrystals also depends on total strain (de Bresser and Spiers, 1997; Laurent et al., 2000) and perhaps on grain size (Gil Sevillano, 2008). Stresses necessary for twinning might also be affected by the presence of second phases, porosity, changes in pore-fluid chemistry, and solid solutes. A comprehensive review of this piezometer has been given by Burkhard (1993).

5.5. Twinning and constitutive behavior

Despite considerable laboratory work, a general constitutive law that includes all relevant state variables is still missing for carbonate rocks (e.g., see discussions by Evans, 2005; Renner and Evans, 2002). At lower temperatures where twinning is prevalent, it is likely that the strength of carbonate rocks will evolve during natural deformation because of hardening owing to twin production and changes in dislocation structures, and recovery resulting from recrystallization, dislocation climb, and cross-slip. A useful scheme to incorporate some of these effects is given by Brown et al. (2012). Detailed descriptions of
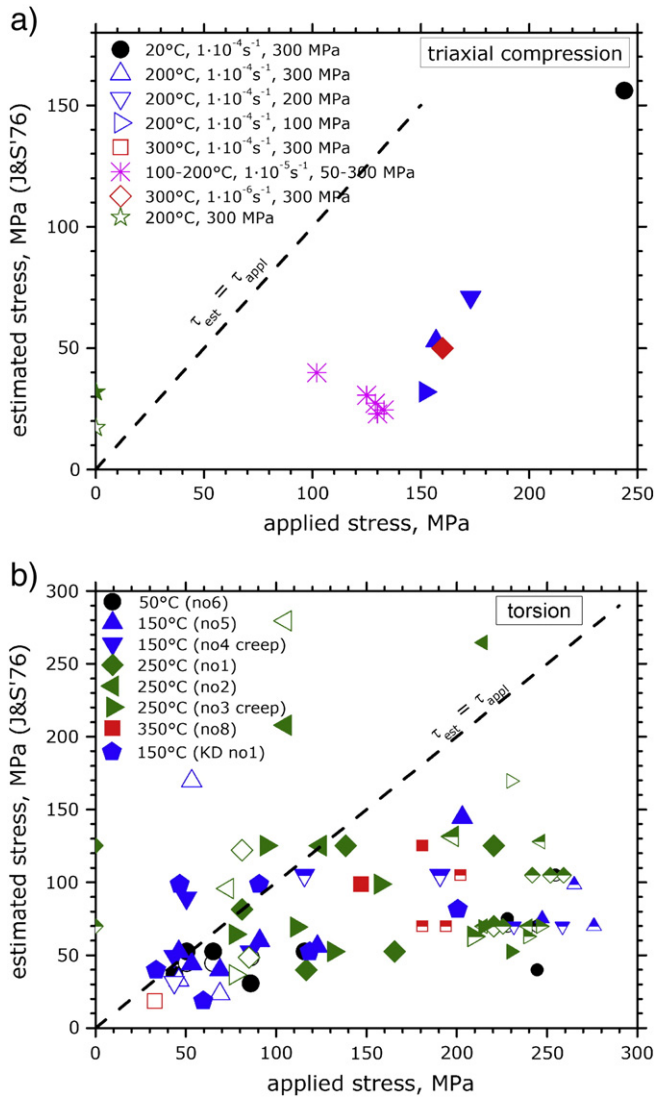
a)

triaxial compression

Legend:
- ● 20°C, $1 \cdot 10^{-4} s^{-1}$, 300 MPa
- △ 200°C, $1 \cdot 10^{-4} s^{-1}$, 300 MPa
- ▽ 200°C, $1 \cdot 10^{-4} s^{-1}$, 200 MPa
- ▷ 200°C, $1 \cdot 10^{-4} s^{-1}$, 100 MPa
- □ 300°C, $1 \cdot 10^{-4} s^{-1}$, 300 MPa
- ✳ 100–200°C, $1 \cdot 10^{-5} s^{-1}$, 50–300 MPa
- ◇ 300°C, $1 \cdot 10^{-6} s^{-1}$, 300 MPa
- ☆ 200°C, 300 MPa

estimated stress, MPa (J&S'76)

applied stress, MPa

$\tau_{est} = \tau_{appl}$

b)

torsion

Legend:
- ● 50°C (no6)
- ▲ 150°C (no5)
- ▼ 150°C (no4 creep)
- ◆ 250°C (no1)
- ◀ 250°C (no2)
- ◀ 250°C (no3 creep)
- ■ 350°C (no8)
- ⬟ 150°C (KD no1)

estimated stress, MPa (J&S'76)

applied stress, MPa

$\tau_{est} = \tau_{appl}$

Fig. 11. Stress estimated using the piezometer of Jamison and Spang (1976) that relates the percentage of twinned grains to the applied equivalent shear stress for triaxial compression (a) and torsion (b) tests. Open symbols represent results of 1 twin set, closed symbols those of 2 sets, and half-filled symbols stress estimates from 3 twin sets. For torsion experiments large size symbols show data from ST-sections and small size symbols from SR-sections, respectively. Dashed lines indicate equality of estimated and applied stress. KD denotes Kunzendorfer marble, all other data are measured on Carrara marble.

the elementary processes involved in twin nucleation, twin growth, and the interactions of matrix dislocations with twin boundaries and twinning dislocations will be an important part of the constitutive law. In particular, detailed knowledge of the relative kinetics of each of the elementary processes is required to predict strength at very slow strain rates. If twin nucleation and twin growth have distinctly different kinetics, then the temperature at which broad twins are most prevalent will also depend on strain rate, a fact which will need to be considered when extrapolating to natural deformation rates.

6. Conclusions

Our experiments extend observations of twin production in carbonates over a larger range of conditions of pressure, temperature, strain and loading conditions. Taken together with extensive previous work on twin production, the data suggest that twin microstucture is affected by at least three parameters, strain, temperature, and peak load.

1. During plastic flow, twin nucleation continues to occur over a broad range of strains. Twin widening may also occur at all temperatures tested, but the rates are reduced at lower temperatures, consistent with the idea of temperature-dependent twin microstructures.
2. Within rather extensive experimental scatter, over the range of $20 < T < 350$ °C, the peak flow strength is roughly proportional to the square root of twin density, N_L, a relation that is consistent with a reduction of the mean free slip length of matrix dislocations.
3. The hardening coefficients in both triaxial compression tests and torsion experiments suggest that twin production contributes to the evolution of strength. As temperature increases, the hardening coefficients are reduced, and concurrently, twin broadening is more prevalent. Taken together these observations suggest that the hardening interactions between twin boundaries and matrix dislocations are reduced at higher T.
4. Dislocation structures within the rocks deformed in this study are suggestive of hardening interactions between twin boundaries and matrix dislocations. Dislocation densities and cell sizes are also roughly consistent with previously suggested microstructural piezometers. Apparently, both twin density and dislocation cell structure are important state variables for describing the strength of these rocks.
5. In mechanical tests on Carrara and Kunzendorfer marbles, the twin frequency was lower than that predicted by the piezometer of Jamison and Spang (1976) at almost all stresses in both torsion loading and conventional triaxial compression.
6. The effect of P and strain rate were not tested here in detail, but given the influence of T, and the possible interaction of hardening and recovery processes, it is entirely possible that the twin microstructure might be influenced by large changes in strain rate.

Further work is necessary to improve the understanding of twin production and its effect on strength. In particular, detailed observations are needed to constrain the effect of changes in temperature, strain and strain rate on the relative contribution of twinning to total strain, on the relative kinetics of twin nucleation and growth, and on the transition from twin production to dislocation creep in the absence of twinning. There are also large uncertainties in the effects of grain size, porosity, second phases, and solid solution on twin production. Improved knowledge of these factors may better constrain the interpretation of microstructures in naturally deformed rocks.

Appendix A

Paterson and Olgaard (2000) discussed the evaluation of torque-twist data measured during confined torsion experiments on cylindrical samples. Our samples for torsion tests were shaped like dog-bones (see Fig. 2), with total length L ($= 30$ mm); diameters varied from $D = 15$ mm at the top and bottom (s1 and s5), to $f \cdot D = 8$ or 10 mm (s3) along the narrow central section, where f denotes the fraction of the maximum diameter D. The fractional length of the central part, denoted by $\alpha \cdot L$, was always 9.2 mm. Adjacent conical parts, s2 and s4, had fractional lengths of $\frac{\beta}{2}L$. The end sections, s1 and s5, each had fractional lengths $\frac{\omega}{2}L$, so that $\alpha + \beta + \omega = 1$. The

total torque over each transverse cross-section, M, is constant, and, thus, the maximum shear stress, τ_{max}, occurs on the outer surface of the transverse section with minimum diameter (s3). If the material deforms by power-law creep,

$$\tau_{max} = M\frac{4(3+1/n)}{\pi(fD)^3}. \tag{A1}$$

Twist is also concentrated in the narrow section, with maximum strain, γ_{max} (bright line in Fig. 2c), occurring at the exterior. To inspect microstructure, we prepared thin sections either transverse to the sample axis (SR) or tangent to the outer cylindrical surface (ST) (Fig. 2b, c).

First, we use a simple extension of Paterson and Olgaard (2000) to treat the effect of non-uniform diameter on the stress-strain distribution. The total twist rate along the entire sample, $\dot{\theta}_T$, is given by integrating the twist rate $d\dot{\theta}_x$ of individual transverse slices of thickness dx and diameter D_x over the sample length, L. For power law creep, (Eq. (17) in Paterson and Olgaard (2000)):

$$\dot{\theta}_T = \int_0^L d\dot{\theta}_x dx = 2A\left\{\frac{4}{\pi}\left(3+\frac{1}{n}\right)\right\}^n M^n e^{-\frac{Q}{RT}}D(x), \text{ with } D(x) = \int_0^L \frac{1}{D_x^{3n+1}}dx. \tag{A2}$$

For our samples, the integral above can be split into 5 sections, s1 to s5,

$$D(x) = \sum_{i=1}^5 D_{si}(x), \text{ where}$$

$$D_{s1}(x) = \int_0^{L\frac{\omega}{2}} [D]^{-(3n+1)}dx$$

$$D_{s2}(x) = \int_{L\frac{\omega}{2}}^{L\frac{(1-\alpha)}{2}} \left[D\left\{1+\frac{1-f}{\beta}\left(\omega-\frac{2x}{L}\right)\right\}\right]^{-(3n+1)}dx,$$

$$D_{s3}(x) = \int_{L\frac{(1-\alpha)}{2}}^{L\frac{(1+\alpha)}{2}} [fD]^{-(3n+1)}dx, \tag{A3}$$

$$D_{s4}(x) = \int_{L\frac{(1+\alpha)}{2}}^{L\left(1-\frac{\omega}{2}\right)} \left[D\left\{1+\frac{1-f}{\beta}\left(\omega-2+\frac{2x}{L}\right)\right\}\right]^{-(3n+1)}dx, \text{ and}$$

$$D_{s5}(x) = \int_{L\left(1-\frac{\omega}{2}\right)}^{L} [D]^{-(3n+1)}dx.$$

Summing gives

$$D(x) = \frac{1}{D^{3n+1}}\left\{\frac{L\omega}{2} + \frac{L\beta}{6n(1-f)}\left(\frac{1}{f^{3n}}-1\right) + \frac{L\alpha}{f^{3n+1}} - \frac{L\beta}{6n(1-f)}\left(1-\frac{1}{f^{3n}}\right) + \frac{L\omega}{2}\right\}$$

$$= \frac{L}{D^{3n+1}}w \text{ with } w = \omega + \frac{\alpha}{f^{3n+1}} + \frac{\beta}{3n(1-f)}\left(\frac{1}{f^{3n}}-1\right). \tag{A4}$$

The total twist is

$$\theta_T = \dot{\theta}_T t = zwL, \text{ with } z = 2A\left\{\frac{4}{\pi}\left(3+\frac{1}{n}\right)\right\}^n M^n \frac{e^{-\frac{Q}{RT}}}{D^{3n+1}}ts. \tag{A5}$$

Fig. A1a shows the normalized twist, θ/θ_T, at any normalized position, x/L, for $L = 30$ mm with $D = 15$ mm at the top and bottom and $f \cdot D = 8$ mm in a reduced central section 9.2 mm long. The twist concentration in s3 increases slightly with increasing stress exponent, n.

Next, we determine γ_x, the normalized shear strain on the sample surface at height, x. Shear strain is normalized by $\gamma_{app} = \theta\frac{D}{2L}$, the maximum strain in a cylinder of similar overall dimensions, but without diameter reduction ($f = 1$). Inserting θ_T (Eq. (A5)) shows that,

$$\gamma_{app} = \frac{D}{2}wz \tag{A6}$$

The strain, γ_x, on the exterior at x, is obtained by differentiating the twist along the x-axis:

$$\gamma_x = \frac{D_x}{2}\frac{d\theta_x}{dx} \tag{A7}$$

Inserting values of D_x and $d\theta_x$, appropriate for sections s1–s5, gives strain contributions of

$$\frac{\gamma_{s1}}{\gamma_{app}} = \frac{1}{w},$$
$$\frac{\gamma_{s2}}{\gamma_{app}} = \frac{1}{w}\left[1+\frac{1-f}{\beta}\left(\omega-2\frac{x}{L}\right)\right]^{-3n},$$
$$\frac{\gamma_{s3}}{\gamma_{app}} = \frac{1}{w}f^{-3n}, \tag{A8}$$
$$\frac{\gamma_{s4}}{\gamma_{app}} = \frac{1}{w}\left[1+\frac{1-f}{\beta}\left(\omega-2+2\frac{x}{L}\right)\right]^{-3n},$$
$$\text{and } \frac{\gamma_{s5}}{\gamma_{app}} = \frac{1}{w}.$$

Strains in s3 are magnified by 1.6–1.7, with more localization for high n (Fig. A1b).

The stress at the sample surface, τ_x, scaled by the maximum stress attained in s3, τ_{max}, is

$$\tau_x = \tau_{max}\left(\frac{fD}{D_x}\right)^3. \tag{A9}$$

Normalizing τ_x to the apparent (maximum) stress τ_{app} at the surface of cylinder with constant diameter ($f = 1$) yields

$$\frac{\tau_x}{\tau_{app}} = \left(\frac{D}{D_x}\right)^3 \text{ since } \frac{\tau_{max}}{\tau_{app}} = \frac{1}{f^3}. \tag{A10}$$

The maximum shear stress in these samples (Fig. A1c) is magnified 6.6-fold.

Next, we determine the strain and stress distribution along the central part of a tangential section (ST) taken at radius r_{ST} (Fig. 2) with diameter D_{ST}. The strain is

$$\gamma_{ST(si)} = \gamma_{si}\frac{D_{ST}}{D_x} \tag{A11}$$

where γ_{si} is the strain in sections s1–s5 from Eq. (A8) and Eq. (A6). In practice, D_{ST} can be determined from W_{ST}, the width of the section at position x with outer diameter D_x by

$$D_{ST} = 2\left\{\left(\frac{D_x}{2}\right)^2 - \left(\frac{W_{ST}}{2}\right)^2\right\}^{1/2}. \tag{A12}$$

The shear stress along the central axis of the ST-section is

$$\tau_{D_{ST}} = \tau_x\left(\frac{D_{ST}}{D_x}\right)^{1/n} = \frac{(D_{ST})^{1/n}}{D_x^{3+1/n}}\left\{\tau_{max}(fD)^3 + k\right\}. \tag{A13}$$

In contrast to the stress on the sample surface, the maximum stress in the ST section depends on n. Assuming that the applied torque is the sum of that sustained by the sample and that supported by the jacket, introduces a correction factor k:

$$k = \frac{3+1/n}{3+1/n_j} \, \tau_j \left(\frac{fDa_j^{3+1/n_j} - fDi_j^{3+1/n_j}}{fDa_j^{1/n_j}} - \left(\frac{\dot{\gamma}_x}{\dot{\gamma}_{fD}} \right)^{1/n_j} \frac{D_x a_j^{3+1/n_j} - D_x i_j^{3+1/n_j}}{D_x a_j^{1/n_j}} \right) \tag{A14}$$

where n_j is the stress exponent for creep of the jacket; τ_j is the maximum shear stress in the jacket in the reduced section. $D_x a_j$ and $D_x i_j$ are the outer and inner jacket diameters at x; and fDa_j and fDi_j are the outer and inner jacket diameters in the reduced section; $\dot{\gamma}_{fD}$ is the (maximum) shear strain rate in the reduced part; and $\dot{\gamma}_x$ is the shear strain rate at position x. The correction is most important when rocks are weak compared to the jacket, e.g., at low-temperatures.

For a radial section (SR) from section s3, shear stress increases with r:

$$\tau_r = \left(\frac{2r}{fD} \right)^{1/n} \tau_{max}. \tag{A15}$$

Replacing τ_{max} by τ_{app} (Eq. (A10)) yields

$$\frac{\tau_r}{\tau_{app}} = \left(\frac{2r}{D} \right)^{1/n} \frac{1}{f^{3+1/n}}. \tag{A16}$$

(Fig. A2a). Thus, shear stress increases strongly with radius, especially for large n. By contrast, shear strain increases linearly with radius:

$$\gamma_r = \frac{2r}{fD} \gamma_{max}. \tag{A17}$$

Using Eq. (A8) to replace γ_{max}, the maximum strain in s3, by γ_{app} gives

$$\frac{\gamma_r}{\gamma_{app}} = \frac{2r}{D} \frac{1}{wf^{3n+1}}. \tag{A18}$$

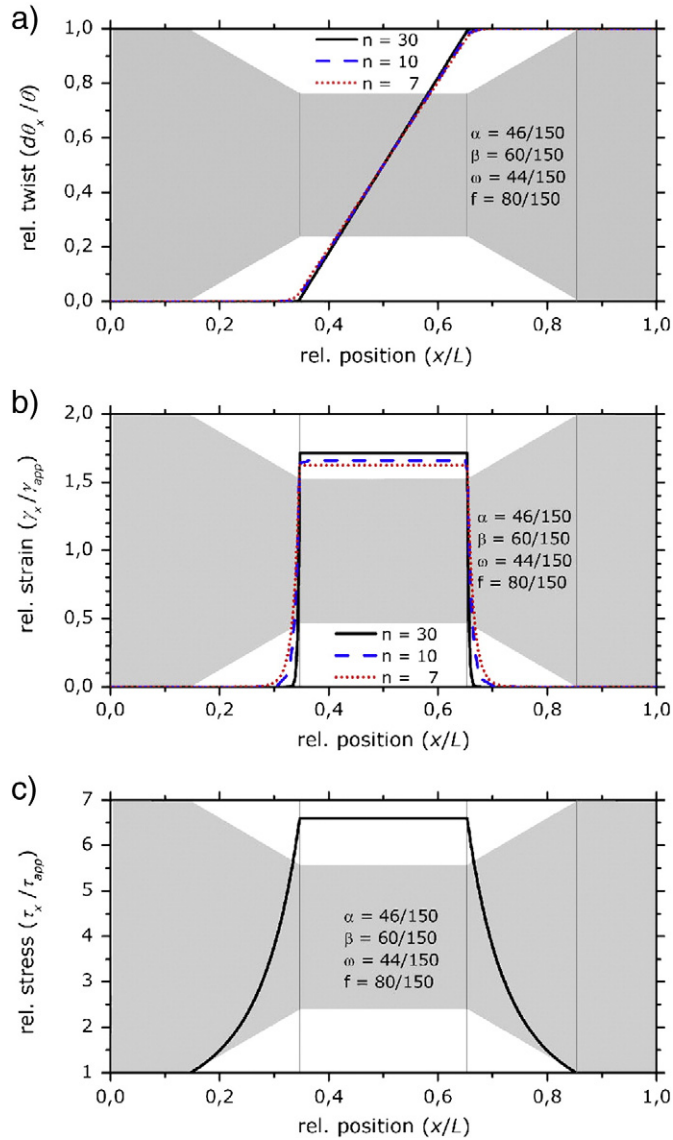Fig. A2b shows the influence of n on localization.

Fig. A1. Distribution of relative normalized twist (a), strain (b), and stress (c) as a function of the relative position x/L for a twisted dog-bone shaped sample. Localization of twist and strain increases slightly with increasing stress exponent n. The fractional dimensions α, β, ω, and f are given for a sample with length L of 30 mm and diameter D of 15 mm, reduced to $f \cdot D = 8$ mm in the central portion of length $\alpha \cdot L = 9.2$ mm.
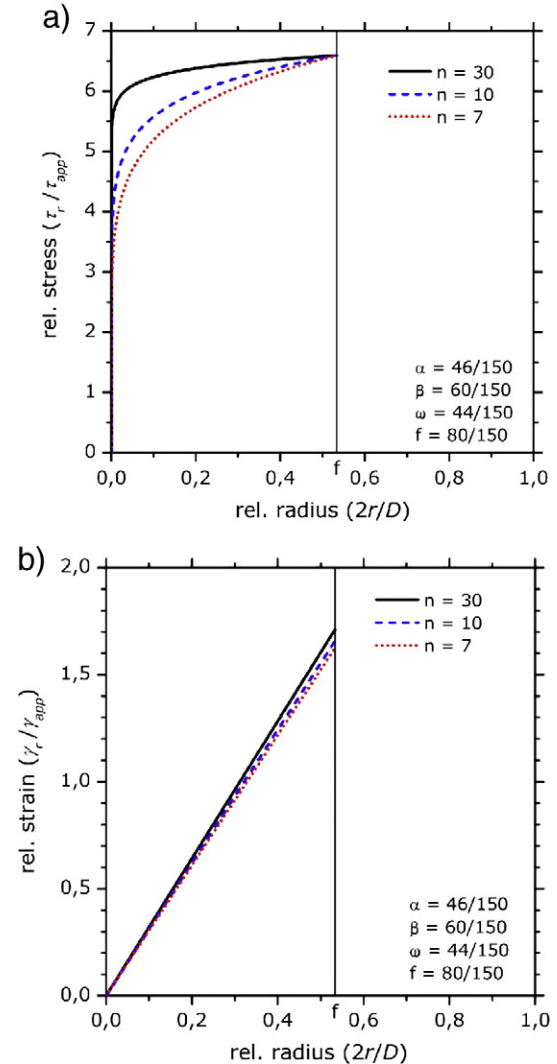

Fig. A2. Increase of relative normalized shear stress (a) and strain (b) as a function of the relative radius $2r/D$ within the radial section SR for various stress exponents n. Sample dimensions are similar to Fig. A1.

References

Ananthakrishna, G., 2007. Current theoretical approaches to collective behavior of dislocations. Physics Reports 440, 113–259.

Astafurova, E.G., Chumlyakov, Y.I., 2009. Strain hardening upon twinning of [$\bar{1}$11], [$\bar{1}$44], and [011] single crystals of hadfield steel. Physics of Metals and Metallography 108, 510–518.

Barber, D.J., Wenk, H.R., 1979. Deformation twinning in calcite, dolomite, and other rhombohedral carbonates. Physics and Chemistry of Minerals 5, 141–165.

Barber, D.J., Wenk, H.R., Gomez-Barreiro, J., Rybacki, E., Dresen, G., 2007. Basal slip and texture development in calcite: new results from torsion experiments. Physics and Chemistry of Minerals 34, 73–84.

Barnett, M.R., 2007. Twinning and the ductility of magnesium alloys. Materials Science and Engineering A 464, 1–7.

Barnett, M.R., Nave, M.D., Ghaderi, A., 2012. Yield point elongation due to twinning in a magnesium alloy. Acta Materialia 60, 1433–1443.

Beyerlein, I.J., Tomé, C.N., 2008. A dislocation-based constitutive law for pure Zr including temperature effects. International Journal of Plasticity 24, 867–895.

Blenkinsop, T., 2000. Deformation Microstructures and Mechanisms in Minerals and Rocks. Kluwer, London.

Brown, D.W., Beyerlein, I.J., Sisneros, T.A., Clausen, B., Tomé, C.N., 2012. Role of twinning and slip during compressive deformation of beryllium as a function of strain rate. International Journal of Plasticity 29, 120–135.

Burkhard, M., 1993. Calcite twins, their geometry, appearance and significance as stress-strain markers and indicators of tectonic regime—a review. Journal of Structural Geology 15, 351–368.

Capolungo, L., Beyerlein, I.J., Kaschner, G.C., Tome, C.N., 2009. On the interaction between slip dislocations and twins in HCP Zr. Materials Science and Engineering A 513–14, 42–51.

Christian, J.W., Mahajan, S., 1995. Deformation twinning. Progress in Materials Science 39, 1–157.

Coli, M., 1989. Litho-structural assemblage and deformation history of Carrara marble. Bollettino della Societa Geologica Italiana 108, 581–590.

Covey−Crump, S.J., Schofield, P.F., 2009. Neutron diffraction and the mechanical behavior of geological materials. In: Liang, L., Rinaldi, R., Schober, H. (Eds.), Neutron Applications in Earth. Springer, Energy and Environmental Sciences, pp. 257–282.

de Bresser, J.H.P., 1996. Steady state dislocation densities in experimentally deformed calcite materials: single crystals versus polycrystals. Journal of Geophysical Research 101, 22189–22201.

de Bresser, J.H.P., 2002. On the mechanism of dislocation creep of calcite at high temperature: inferences from experimentally measured pressure sensitivity and strain rate sensitivity of flow stress. Journal of Geophysical Research 107, 2337. http://dx.doi.org/10.1029/B122002JB001812.

de Bresser, J.H.P., Spiers, C.J., 1993. Slip Systems in calcite single crystals deformed at 300–800 °C. Journal of Geophysical Research 98, 6397–6409.

de Bresser, J.H.P., Spiers, C.J., 1997. Strength characteristics of the r, f, and c slip systems in calcite. Tectonophysics 272, 1–23.

Dehoff, R.T., Rhines, F.N., 1961. Determination of number of particles per unit volume from measurements made on random plane selections—the general cylinder and the ellipsoid. Transactions of the Metallurgical Society of AIME 221, 975–982.

Edmond, J.M., Paterson, M.S., 1972. Volume changes during the deformation of rocks at high pressure. International Journal of Rock Mechanics and Mining Sciences 9, 161–182.

Evans, B., 2005. Creep constitutive laws for rocks with evolving structure. In: Bruhn, D., Burlini, L. (Eds.), High-Strain Zones: Structure and Physical Properties. Geolog. Soc. of London, London, pp. 329–346.

Ferrill, D.A., 1991. Calcite twin widths and intensities as metamorphic indicators in natural low-temperature deformation of limestone. Journal of Structural Geology 13, 667–675.

Ferrill, D.A., 1998. Critical re-evaluation of differential stress estimates from calcite twins in coarse-grained limestone. Tectonophysics 285, 77–86.

Ferrill, D.A., Morris, A.P., Evans, M.A., Burkhard, M., Groshong Jr., R.H., Onasch, C.M., 2004. Calcite twin morphology: a low-temperature deformation geothermometer. Journal of Structural Geology 26, 1521–1529.

Fischer, G.J., Paterson, M.S., 1989. Dilatancy during rock deformation at high temperatures and pressures. Journal of Geophysical Research 94, 17,607–17,617.

Fredrich, J., Evans, B., 1989. Micromechanics of the brittle to plastic transition in Carrara marble. Journal of Geophysical Research 94, 4129–4145.

Friedman, M., Heard, H.C., 1974. Principal stress ratios in Cretaceous limestones from Texas Gulf Coast. American Association of Petroleum Geologists Bulletin 58, 71–78.

Garber, R.I., 1947. Mechanism of twinning in calcite and sodium nitrate during plastic deformation. Zhur. Eksptl. i Teoret. Fiz. 17, 48–62.

Gil Sevillano, J., 2008. Geometrically necessary twins and their associated size effects. Scripta Materialia 59, 135–138.

Gil Sevillano, J., de las Cuevas, F., 2012. Internal stresses and the mechanism of work hardening in twinning-induced plasticity steels. Scripta Materialia 66, 978–981.

Groshong Jr., R.H., 1972. Strain calculated from twinning in calcite. Geological Society of America Bulletin 83, 2025–2037.

Groshong Jr., R.H., 1974. Experimental test of least-squares strain gage calculation using twinned calcite. Geological Society of America Bulletin 85, 1855–1864.

Groshong Jr., R.H., 1988. Low-temperature deformation mechanisms and their interpretation. Geological Society of America Bulletin 100, 1329–1360.

Groshong Jr., R.H., Teufel, L.W., Gasteiger, C., 1984. Precision and accuracy of the calcite strain-gage technique. Geological Society of America Bulletin 95, 357–363.

Gutierrez-Urrutia, I., Raabe, D., 2011. Dislocation and twin substructure evolution during strain hardening of an Fe–22wt.% Mn–0.6wt.% C TWIP steel observed by electron channeling contrast imaging. Acta Materialia 59, 6449–6462.

Gutierrez-Urrutia, I., Raabe, D., 2012. Grain size effect on strain hardening in twinning-induced plasticity steels. Scripta Materialia 66, 992–996.

Heard, H.C., 1960. Transition from brittle to ductile flow in Solnhofen limestone as a function of temperature, confining pressure, and interstitial fluid pressure. In: Griggs, D., Handin, J. (Eds.), Rock deformation. Geol. Soc. Am. Mem., New York, pp. 193–226.

Jamison, W.R., Spang, J.H., 1976. Use of calcite twin lamellae to infer differential stress. Geological Society of America Bulletin 87, 868–872.

Janssen, C., Romer, R.L., Hoffmann-Rothe, A., Kesten, D., Al-Zubi, H., 2004. The Dead Sea transform: evidence for a strong fault? Journal of Geology 112, 561–575.

Karato, S., 2008. Deformation of Earth Materials—An Introduction to the Rheology of Solid Earth. Cambridge Univ. Press, Cambridge.

Kennedy, L., White, J., 2001. Low-temperature recrystallization in calcite: mechanisms and consequences. Geology 29, 1027–1030.

Klassen-Neklyudova, 1964. Mechanical Twinning of Crystals. Consultants Bureau, New York.

Kocks, U.F., Tome, C.N., Wenk, H.R., 1998. Texture and Anisotropy: Preferred Orientations in Polycrystals and Their Effect on Materials Properties. Cambridge Univ. Press, Cambridge.

Kohlstedt, D.L., Weathers, M.S., 1980. Deformation-induced microstructures, paleopiezometers, and differential stresses in deeply eroded fault zones. Journal of Geophysical Research 85, 6269–6285.

Lacombe, O., 2007. Comparison of paleostress magnitudes from calcite twins with contemporary stress magnitudes and frictional sliding criteria in the continental crust: mechanical implications. Journal of Structural Geology 29, 86–99.

Lacombe, O., Laurent, P., 1992. Determination of principal stress magnitudes using calcite twins and rock mechanics data. Tectonophysics 2002, 83–93.

Laurent, P., Bernard, P., Vasseur, G., Etchecopar, A., 1981. Stress tensor determination from the study of e twins in calcite: a linear programming method. Tectonophysics 78, 651–660.

Laurent, P., Kern, H., Lacombe, O., 2000. Determination of deviatoric stress tensors based on inversion of calcite twin data from experimentally deformed monophase samples. Part II. Axial and triaxial stress experiments. Tectonophyis. 327, 131–148.

Li, Y.S., Zhang, Y., Tao, N.R., Lu, K., 2009. Effect of the Zener–Hollomon parameter on the microstructures and mechanical properties of Cu subjected to plastic deformation. Acta Materialia 57, 761–772.

Marinelli, M.C., Degallaix, S., Alvarez-Armas, I., 2006. Dislocation structure developed in the austenitic-phase of SAF 2507 duplex stainless steel. Materials Science and Engineering A 435–436, 305–308.

Masuda, T., Miyake, T., Kimura, N., Okamoto, A., 2011. Application of the microboudin method to paleodifferential stress analysis of deformed impure marbles from Syros, Greece: implications for grain-size and calcite-twin paleopiezometers. Journal of Structural Geology 33, 20–31.

Molli, G., White, J.C., Kennedy, L., Taini, V., 2011. Low-temperature deformation of limestone, Isola Palmaria, northern Apennine, Italy—the role of primary textures, precursory veins and intracrystalline deformation in localization. Journal of Structural Geology 33, 255–270.

Nicolas, J., Poirier, J.P., 1976. Crystalline Plasticity and Solid State Flow in Metamorphic Rocks. Wiley, London.

Passchier, C.W., Trouw, R.A.J., 1996. Microtectonics. Springer, Berlin.

Paterson, M.S., 1970. A high-pressure, high-temperature apparatus for rock deformation. International Journal of Rock Mechanics and Mining Sciences & Geomechanics Abstracts 7, 517–526.

Paterson, M.S., Olgaard, D.L., 2000. Rock deformation tests to large shear strains in torsion. Journal of Structural Geology 22, 1341–1358.

Poirier, J.P., 1985. Creep of Crystals: High-Temperature Deformation Processes in Metals, Ceramics, and Minerals. Cambridge Univ. Press, London.

Renner, J., Evans, B., 2002. Do calcite rocks obey the power law creep equation? In: de Meer, S., Drury, M.R., de Bresser, J.H.P., Pennock, G. (Eds.), Deformation Mechanisms, Rheology, Tectonics. : Current Status Future Perspectives. Geol. Soc. London, London, pp. 309–329.

Renner, J., Evans, B., Siddiqi, G., 2002. Dislocation creep of calcite. Journal of Geophysical Research 107, 2364. http://dx.doi.org/10.1029/2001JB001680.

Reusch, E., 1867. Über eine besondere Gattung von Durchgängen im Steinsalz und Kalkspath. Annalen der Physik 208, 441–451.

Rowe, D.W., Rutter, E., 1990. Palaeostress estimation using calcite twinning: experimental calibration and application to nature. Journal of Structural Geology 12, 1–17.

Rutter, E., 1972. The effects of strain-rate changes on the strength and ductility of Solnhofen limestone at low temperatures and confining pressures. International Journal of Rock Mechanics and Mining Sciences 9, 183–189.

Rutter, E., 1972. The influence of interstitial water on the rheological behaviour of calcite rocks. Tectonophysics 14, 13–33.

Rutter, E., 1974. Influence of temperature, strain rate and interstitial water in experimental deformation of calcite rocks. Tectonophysics 22, 311–334.

Rybacki, E., Evans, B., 1999. Semibrittle flow in Carrara marble at 273–673 K. In: Dresen, G., Handy, M., Janssen, C. (Eds.), Conference on Deformation Mechanisms, Rheology, Microstructures, Neustadt an der Weinstrasse, 1999: Proceedings., GFZ, Potsdam, p. 133.

Rybacki, E., Paterson, M.S., Wirth, R., Dresen, G., 2003. Rheology of calcite–quartz aggregates deformed to large strain in torsion. Journal of Geophysical Research 108, 2089. http://dx.doi.org/10.1029/2002JB001833.

Sakaguchi, A., Sakaguchi, H., Nishiura, D., Nakatani, M., Yoshida, S., 2011. Elastic stress indication in elastically rebounded rock. Geophysical Research Letters 38, L09316.

Tullis, T.E., 1980. The use of mechanical twinning in minerals as a measure of shear stress magnitudes. Journal of Geophysical Research 85, 6263–6268.

Turner, F.J., 1953. Nature and dynamic interpretation of deformation lamellae in calcite of three marbles. American Journal of Science 251, 276–298.

Turner, F.J., 1964. Some geometric aspects of experimentally induced twinning in minerals. In: Reed-Hill, R.E., Hirth, J.P., Rogers, H.C. (Eds.), Conference on Deformation Twinning, Gainesville Florida, 1963, Proceedings. Gordon and Breach Science Publishers, New York, pp. 156–175.

Turner, F.J., Griggs, D., Heard, H.C., 1954. Experimental deformation of calcite crystals. Geological Society of America Bulletin 65, 883–934.

Underwood, E.E., 1970. Quantitative Stereology. Addison-Wesley, Reading, MA.

Wenk, H.R., Barber, D., Reeder, R., 1983. Microstructures in carbonates. In: Reeder, R. (Ed.), Carbonates: Mineralogy and Chemistry. Am. Miner. Soc., Washington DC, pp. 301–369.

Wenk, H.R., Rybacki, E., Dresen, G., Lonardelli, I., Barton, N., Franz, H., Gonzalez, G., 2006. Dauphiné twinning and texture memory in polycrystalline quartz. Part 1: experimental deformation of novaculite. Physics and Chemistry of Minerals 33, 667–676.

Williams, A.J., Cahn, R.W., 1964. The dynamics of elastic twinning in calcite. In: Reed-Hill, R.E., Hirth, J.P., Rogers, H.C. (Eds.), Conference on Deformation Twinning, Gainesville Florida, 1963, Proceedings. Gordon and Breach Science Publishers, New York, pp. 192–208.

Wirth, R., 2004. Focused ion beam (FIB): a novel technology for advanced application of micro- and nanoanalysis in geosciences and applied mineralogy. European Journal of Mineralogy 16, 863–876.

Wirth, R., 2009. Focused ion beam (FIB) combined with SEM and TEM: advanced analytical tools for studies of chemical composition, microstructure and crystal structure in geomaterials on a nanometre scale. Chemical Geology 261, 217–229.

Xiao, G.H., Tao, N.R., Lu, K., 2008. Effects of strain, strain rate and temperature on deformation twinning in a Cu–Zn alloy. Scripta Materialia 59, 975–978.